

Shortwave radiative flux variability through the lens of the Pacific Decadal Oscillation

Boriana Chtirkova¹, Doris Folini¹, Lucas Ferreira Correa¹, and Martin Wild¹

¹ETH Zürich

December 3, 2023

Abstract

The variability of the shortwave radiative fluxes at the surface and top of atmosphere (TOA) is examined in a pre-industrial modelling setup using the Pacific Decadal Oscillation (PDO) as a possible pacemaker of atmospheric decadal-scale variability. Within models from the Coupled Model Intercomparison Project – Phase 6, downwelling shortwave radiation at the surface, the net shortwave fluxes at the surface and TOA, as well as cloud radiative effects show remarkably similar patterns associated with the PDO. Through ensemble simulations designed with a pure PDO pattern in the North Pacific only, we show that the PDO relates to about 20-40% of the unforced year-to-year variability of these shortwave fluxes over the Northern Hemispheric continents. The SST imprint on shortwave-flux variability over land is larger for spatially aggregated time series as compared to smaller areas, due to the blurring effect of small-scale atmospheric noise. The surface and TOA radiative flux anomalies associated with the PDO index range of $[-1.64; 1.64]$ are estimated to reach up to $\pm 6 \text{ Wm}^{-2}$ for North America, $[?] 3 \text{ Wm}^{-2}$ for India and $+2 \text{ Wm}^{-2}$ for Europe. We hypothesise that the redistribution of clouds in response to a North Pacific PDO anomaly can impact the South Pacific and North Atlantic SSTs.

Shortwave radiative flux variability through the lens of the Pacific Decadal Oscillation

Boriana Chtirkova¹, Doris Folini¹, Lucas Ferreira Correa¹, Martin Wild¹

¹Institute for Atmospheric and Climate Sciences, ETH Zürich, Zürich, Switzerland

Key Points:

- The PDO is a prominent pacemaker for variability, accounting for about 1/3 of the shortwave flux year-to-year variability over NH continents.
- A negative PDO anomaly leads to a reduction in atmospheric shortwave reflectivity (clouds) in North America and Europe and an increase in India.
- The redistribution of clouds in response to a North Pacific PDO anomaly might influence SSTs in the South Pacific and North Atlantic.

Corresponding author: Boriana Chtirkova, boriana.chtirkova@env.ethz.ch

Abstract

The variability of the shortwave radiative fluxes at the surface and top of atmosphere (TOA) is examined in a pre-industrial modelling setup using the Pacific Decadal Oscillation (PDO) as a possible pacemaker of atmospheric decadal-scale variability. Within models from the Coupled Model Intercomparison Project – Phase 6, downwelling shortwave radiation at the surface, the net shortwave fluxes at the surface and TOA, as well as cloud radiative effects show remarkably similar patterns associated with the PDO. Through ensemble simulations designed with a pure PDO pattern in the North Pacific only, we show that the PDO relates to about 20-40% of the unforced year-to-year variability of these shortwave fluxes over the Northern Hemispheric continents. The SST imprint on shortwave-flux variability over land is larger for spatially aggregated time series as compared to smaller areas, due to the blurring effect of small-scale atmospheric noise. The surface and TOA radiative flux anomalies associated with the PDO index range of $[-1.64; 1.64]$ are estimated to reach up to $\pm 6 \text{ Wm}^{-2}$ for North America, $\mp 3 \text{ Wm}^{-2}$ for India and $\pm 2 \text{ Wm}^{-2}$ for Europe. We hypothesise that the redistribution of clouds in response to a North Pacific PDO anomaly can impact the South Pacific and North Atlantic SSTs.

Plain Language Summary

We investigate how solar radiation at Earth’s surface and the top of the atmosphere, which are mainly controlled by cloudiness, can vary over decades as a response to a horseshoe pattern typical for the North Pacific sea surface temperatures (SSTs) – the Pacific Decadal Oscillation (PDO). We use idealized climate model simulations to show that about a third of the year-to-year changes in solar radiation over the Northern Hemispheric continents are related to this phenomenon. These changes are more noticeable when looking at large areas rather than small ones, as high frequency smaller scale atmospheric variations can obscure the bigger picture. By keeping the PDO fixed to a constant negative value, implying below average cold sea surface temperatures off the western coast of North America and warmer than average temperatures towards Japan, we show that North America and Europe exhibit a reduction in cloudiness, while clouds increase in India. The same with an opposite sign is true for a positive PDO anomaly. These changes in cloud patterns might further affect SSTs in the South Pacific and North Atlantic oceans.

1 Introduction

Internal climate variability on a range of spatial and temporal scales and its interplay with radiative processes is important for understanding Earth’s energy balance and its potential response to changing forcings over different temporal and spatial scales. The shortwave part of Earth’s energy budget, specifically absorbed solar radiation (or net shortwave flux at the top of atmosphere, TOA) and its response to greenhouse gas forcing are shown to be fundamental for Earth’s climate and climate change (Trenberth & Fasullo, 2009; Donohoe et al., 2014). From a surface perspective, aerosols and their temporal variability are suggested to impact the surface energy balance by altering downwelling shortwave radiation at the surface (e.g. Stanhill and Moreshet (1992); Wild (2009); Wild et al. (2012, 2014)).

Several studies have shown that internal climate variability interferes with the energy fluxes on a range of scales, notably including decadal time scales at TOA (e.g. Allan et al. (2014); Loeb et al. (2018, 2021); Wills et al. (2021); Meyssignac et al. (2023)) and at the surface (e.g. Folini et al. (2017); Augustine and Capotondi (2022); Chtirkova et al. (2023)). Variations are shown to relate to known elements of internal variability like El Niño–Southern Oscillation (ENSO), Pacific Decadal Oscillation (PDO), Atlantic Multidecadal Oscillation (AMO). The focus of our study is the PDO, which is identified as the dominant pattern of sea surface temperature variability in the North Pacific, characterised by decadal-scale warming and cooling with a characteristic horseshoe pattern

(Mantua & Hare, 2002). Over decadal time scales, the PDO is associated with strengthening and expansion of the North Pacific subpolar gyre in response to a deepening of the Aleutian Low and increasing variability at longer time scales due to adjustment of westward propagating oceanic Rossby waves (Qiu et al., 2007; Taguchi et al., 2007; Wills et al., 2019). The PDO has a South Pacific counterpart, referred to as South Pacific Decadal Oscillation (SPDO, Chen and Wallace (2015); IPCC (2021)), which is thought to be influenced by a collection of processes including extratropical modes, ENSO teleconnections and ocean dynamics (Shakun & Shaman, 2009; Zhang et al., 2018). The combined phenomenon between PDO, ENSO and SPDO, though believed to be physically distinct modes (Newman et al., 2016; IPCC, 2021), is the Inter-decadal Pacific Oscillation (IPO, Power et al. (1999); Folland (2002); Henley et al. (2015)).

The PDO is found to be related to atmospheric dynamics, specifically the Pacific North American pattern, and is strongly correlated with temperature and precipitation patterns over North America (Liu et al., 2017; Rohli et al., 2022). There are further indications of a possible link between the Pacific North American Pattern and North Atlantic Oscillation and Atlantic storm tracks through baroclinic waves (Pinto et al., 2010). The PDO has also been proposed as the major driver of decadal-scale surface downwelling shortwave radiation anomalies (dimming and brightening) for the United States (Augustine & Capotondi, 2022) and is also hypothesised as a contributor to European dimming and brightening (Chtirkova et al., 2023).

In this study, we focus on various aspects of the shortwave part of Earth’s energy budget, including the downwelling shortwave radiation at the surface – F_S^\downarrow , net shortwave radiation at the top of the atmosphere (TOA, positive downward) – $F_T^{\downarrow\uparrow}$, net shortwave radiation at Earth’s surface (positive downward) – $F_S^{\downarrow\uparrow}$, shortwave atmospheric absorption – A_{atm} , and the shortwave cloud radiative effects at the surface and TOA – CRE_S , CRE_T . As our interest is with the PDO as a potential pacemaker of part of the internal variability of shortwave fluxes for decadal scales, we use the PDO evolution as a reference and examine the shortwave fluxes “through the lens of the PDO”. We do so by analysing both coupled climate model simulations from the Coupled model intercomparison project – Phase 6 (CMIP6, Eyring et al. (2016)) and our own simulations with the atmosphere-only global climate model ICON, where we constrain the PDO spatial anomaly to a specific value and assess the response of the shortwave radiative fluxes. The paper is structured as follows: in section 2 we describe the data and experimental setup. The results are presented in three parts: in section 3.1, we identify patterns of decadal trends in the shortwave fluxes; in section 3.2, we estimate the fraction of total variability attributable to SSTs and PDO and in section 3.3 we quantify the anomalies in the radiative fluxes as a function of the PDO index value. In section 4, we discuss potential differences that arise from the lack of coupling or from using specifically ICON-A, we also bring observed PDO anomalies into the picture. We conclude in section 5.

2 Data and Methods

The study consists of two parts – we use coupled model data to pinpoint the qualitative relationship between the SW fluxes and PDO and we give a quantification of the fraction of variability attributable to PDO and the flux anomalies in Wm^{-2} based on our own numerical simulations.

2.1 CMIP6 Data

The first part of the study uses the unforced control simulations (piControl) of CMIP6 (Eyring et al., 2016) to investigate the unforced variability of the shortwave fluxes at the surface and TOA and relate them to the PDO. The PDO index for the CMIP6 analysis is computed using the the Climate Variability Diagnostics Package—CVDP, version 5.1.1 (Phillips et al., 2014), developed by NCAR’s Climate Analysis Section. We include

112 52 simulations from 44 coupled models. The multiple simulations for some models come
 113 from slightly modified model versions in terms of physical parameterizations used or as
 114 different realizations. The full list is given in Table 1. Our analysis uses annual mean
 115 data, and is performed on a per grid box level. The radiative fluxes are interpolated to
 116 a 1° grid (same as the GFDL-ESM4 grid) using 2nd order conservative remapping. This
 117 part is an expansion of Chtirkova et al. (2023) to all short shortwave fluxes: for each of
 118 the 52 simulations, we use annual mean data to compute the distribution of all possi-
 119 ble trends (linear regressions) in the PDO index, then we take the periods with trend
 120 magnitudes below the 10th and above the 90th percentile and combine them into com-
 121 posite (mean) trend maps of the shortwave fluxes – one for the increasing and one for
 122 the decreasing phases of the PDO, subsequently combining individual models into multi-
 123 model median maps, one per shortwave flux component. In addition, to provide a region
 124 specific discussion, we select four regions by visual inspection of the shortwave flux trend
 125 maps (that are derived from PDO index trends), focusing on regions that do show trends
 126 upon strong changes of the PDO. We choose regions with approximately equal area (be-
 127 tween 3.7 and 3.9 10⁶ km²). The regions we come up are the following and we refer to
 128 them with the names of the nearest (but not the whole) geographical features they cover:
 129 North America (30-50°N, 250-270°E), Europe (40-55°N, 0-30°E), India and Indochinese
 130 Peninsula (10-18°N, 71-110°E) and Australia (15-30°S, 128-150°E). A visual depiction
 131 of the regions is provided on the last subplot of Figure 2.

132 2.2 ICON-A simulations

133 We use the atmospheric part of the icosahedral nonhydrostatic (ICON) Earth Sys-
 134 tem Model (ESM): ICON-A (Jungclaus et al., 2022). The atmospheric general circula-
 135 tion model ICON-A (Giorgetta et al., 2018; Crueger et al., 2018) is in a configuration
 136 using the Max Planck Institute climate physics package and the rotated R2B4 grid (grid
 137 id 0013), the same as in the ICON-ESM-LR CMIP6 data with an approximate grid in-
 138 crement of 160 km. The tuning configuration is also the same as in the coupled version’s
 139 piControl simulation. As boundary conditions, we use monthly mean SST data from the
 140 first 100 (out of 500) years coupled simulation within CMIP6. The SST climatological
 141 mean fields for the simulations as well as sea ice climatologies are computed over all 500-
 142 years of ICON-ESM-LR data. All other boundary conditions are kept at pre-industrial
 143 climatological values, including sea ice data, stratospheric ozone and aerosol optical prop-
 144 erties. Well-mixed greenhouse gasses have a constant vertical mixing ratio and the so-
 145 lar constant is kept at 1360.744 Wm⁻² in accordance with CMIP6 protocols. Our mo-
 146 tivation for using SST data from the coupled CMIP6 run instead of observed data is two-
 147 fold: (1) we have 500 years of statistics that are not contaminated by global warming
 148 and (2) the SST field is in part characteristic of the atmospheric circulation. By using
 149 SSTs from the coupled counterpart of the same model, we avoid a possible mismatch be-
 150 tween the SST data and the specifics of the atmospheric circulation of the ICON model
 151 its R2B4 grid.

152 We run experiments with prescribed SSTs, where we retain only the low-frequency
 153 component of the PDO. This is done by first decomposing the SST field (500-years of
 154 ICON-ESM-LR) into eigenvectors (empirical orthogonal functions, EOFs), eigenvalues
 155 and their principal components (PCs). Following the recommendations of NCAR Cli-
 156 mate Data Guide (Schneider et al., 2013), we deseasonalize and decompose the SST field
 157 in a rectangular box in the North Pacific. The box boundaries are taken from the CVDP
 158 source code (which we use for the CMIP6 analysis). The EOF decomposition is done us-
 159 ing the Python package: pyEOF (Zheng, 2021), which uses the Numpy singular value
 160 decomposition methods (Harris et al., 2020). The PDO is defined as the first principal
 161 component (PC₁, the one with the largest eigenvalue) of the decomposed field – Figure
 162 1 shows the eigenvector expressed as correlation (a), its corresponding time series (b) and
 163 power spectra (c). We further low-pass filter the principal component time series using
 164 a logarithmic function in frequency space with a time window of 10 years. To obtain a

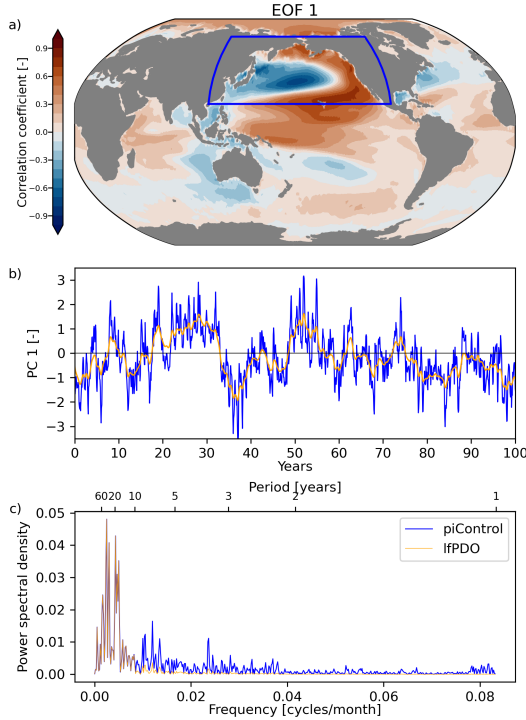


Figure 1. First eigenvector and PC time series derived from EOF analysis of the SST field in ICON-ESM-LR’s piControl run. The first EOF (eigenvector), shown in (a), is presented as the correlation with the monthly SST time series for each grid box. Blue box shows the region in which the EOF decomposition is done. In (b), the normalized value of the original first PC (PDO index) time series is displayed in blue and its low-pass filtered counterpart in orange. Shown are only the first 100 years. Low pass filtering is done by smoothing out frequencies of larger than 1/10 years with a sharp logarithmic function. Panel (c) displays the power spectral density estimated using Welch’s method (Welch, 1967) for the entire 500-year simulation.

165 complete SST field as model boundary conditions, we re-project the resulting low-frequency
 166 time series (lfpDO) on the PDO eigenvector and add the per-grid box seasonal cycle on
 167 top. We do not sum up the remaining eigenvectors and principal components, giving us
 168 an SST field, where the only inter-annual variability comes from the PDO pattern. All
 169 grid boxes outside the PDO box are kept at their climatological values, apart from a smooth-
 170 ing distance around the box which is included for numerical considerations and detailed
 171 in the Appendix Appendix A.

172 To better carve out variability related to SST variability in general and SST vari-
 173 ability related to the PDO in particular, we run two main sets of simulations with 20 en-
 174 semble members each: a set of 100-year simulations where the SST field is taken as is
 175 from the first 100-years of the piControl run (“allSST”) and another set of 100-year sim-
 176 ulations where the only variability in the SST field comes from the low frequency com-
 177 ponent of the PDO obtained as described above via low-pass filtering and projecting the
 178 PC₁ time series (“lfpDO”). Ensemble members share the initialization of the atmosphere
 179 but differ in the calendar day and associated insolation at simulation start (e.g. January
 180 1, January 5 etc.). We discard the first 1-5 years after initialization, considering this as
 181 model spin up, and analyze only subsequent data. This data corresponds to simulation
 182 years 4006-4099 of the ICON-ESM-LR piControl run (95 years in total).

183 To further quantify the influence of a concrete PDO phase (index value) on the SW
 184 fluxes, we run seven 100-year simulations with a “perpetual” PDO phase with different
 185 amplitudes of the SST anomaly and analyse the last 95-years to reduce the impact of
 186 the initial condition. To obtain the field, we take the 99th, 95th and 68th percentiles of
 187 the distribution of monthly PDO index values from the 500-year ICON-ESM-LR CMIP6
 188 piControl simulation, and project constant time series with these index values onto the
 189 PDO eigenvector, seasonality is added on top. The seven PDO index values we consider
 190 based on the above mentioned percentiles and their negative counterparts are 2.58, 1.64,
 191 0.44, 0, -0.44, -1.64 and -2.58. SST anomalies that correspond to these values are fur-
 192 ther detailed in the Appendix Appendix A.

193 3 Results

194 We examine the impact of the PDO on the various shortwave flux components. Each
 195 subsection takes a different perspective in terms of time scales (decadal scale trends and
 196 year-to-year variability) and with regard to the details of the PDO. Section 3.1 looks at
 197 the PDO arising in fully coupled CMIP6 piControl simulations, where it combines with
 198 other modes of variability, and asks about the imprint of strong PDO phase changes on
 199 decadal scale trends of the various shortwave fluxes. Sections 3.2 and 3.3, by contrast,
 200 look at a PDO the pattern of which is highly idealized by design, comprising only the
 201 North Pacific region. Associated atmosphere-only simulations with the ICON-A model
 202 are used to examine the imprint of this idealized PDO on shortwave fluxes: how the year-
 203 to-year variability of the PDO mirrors in shortwave flux time series (3.2) and how short-
 204 wave fluxes differ between ever-lasting positive and negative PDO phases, respectively
 205 (3.3). The latter experiments offer an idealized view on strong PDO phase changes.

206 3.1 Patterns related to PDO

207 Our first quest is to investigate the patterns of the shortwave radiative flux com-
 208 ponents related to PDO phase shifts within CMIP6 models. The analysis is done for the
 209 distribution of all possible 20-year trends (linear regressions) of the PDO index, select-
 210 ing the periods with strongest transitioning of the index and computing the trends of
 211 the energy balance components for those periods (same as in Chtirkova et al. (2023) for
 212 F_S^\downarrow). The strongest transitions of the PDO index in our case correspond to 20-year trends
 213 above 90th and below 10th percentiles for PDO \uparrow and PDO \downarrow transitions respectively. The
 214 results are presented in Figures 2 and 3. For simplicity, we only discuss results related
 215 to PDO \uparrow in the text, i.e. the PDO changing phase from negative to positive, bearing in
 216 mind that the same is valid with opposite sign for the opposite transition.

217 For the all-sky shortwave fluxes, we find that the patterns are remarkably similar
 218 both in spatial structure and in magnitude for F_S^\downarrow and the net shortwave fluxes at the
 219 surface and TOA (F_S^\downarrow , F_T^\downarrow). This suggest that the reduction of F_S^\downarrow (in N. America and
 220 Europe during PDO \uparrow) is also associated with a reduction in F_T^\downarrow and in F_S^\downarrow , i.e. less short-
 221 wave radiation absorbed over these regions by the whole system and in particular – at
 222 Earth’s surface. A significantly different pattern is displayed by shortwave atmospheric
 223 absorption (A_{atm}). Regions bearing a statistically significant imprint (no hatching) of
 224 the PDO phase shift in A_{atm} may not show up in the other shortwave fluxes and vice
 225 versa (e.g. parts of Africa or the Americas). Regions featuring a statistically significant
 226 impact from PDO phase changes may show opposite signs for A_{atm} than for the other
 227 shortwave fluxes. This is notably the case in wide parts of the Pacific and neighbour-
 228 ing regions. For example, the increase in F_T^\downarrow over Australia combines with a reduction
 229 in A_{atm} to result in an even stronger increase in F_S^\downarrow downward.

230 On the clear-sky side (Figure 3), patterns are overall least pronounced for $F_{T,cs}^\downarrow$.
 231 The much more pronounced and geographically more extended patterns in $F_{S,cs}^\downarrow$ and $A_{\text{atm},cs}$

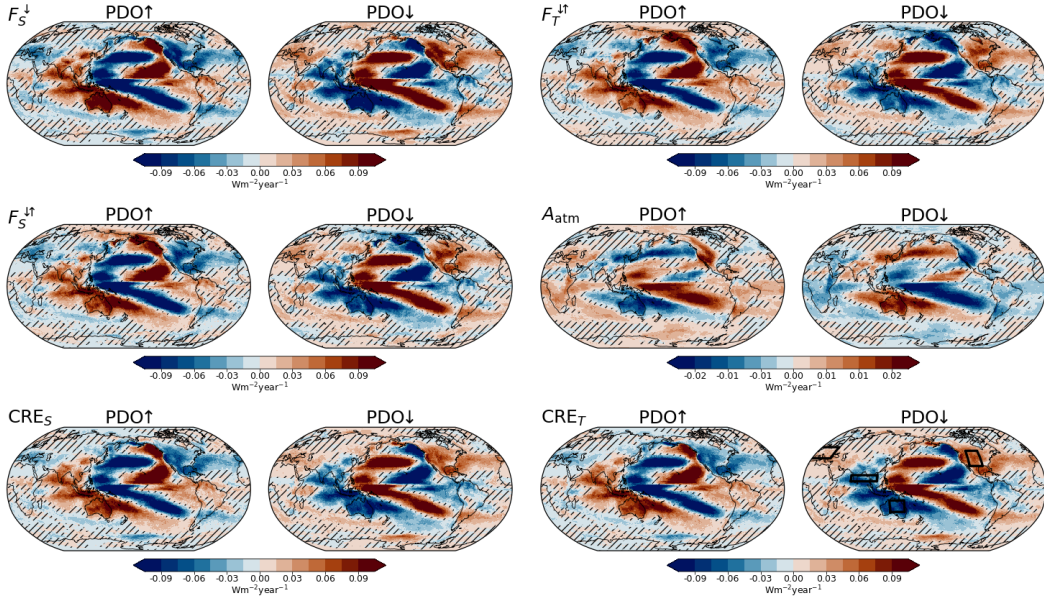


Figure 2. All-sky shortwave flux and cloud radiative effect trend patterns during 20-year periods with a strong negative-to-positive phase transition of the PDO index (PDO↑) and periods with a strong positive-to-negative transition (PDO↓) obtained from CMIP6 piControl simulations. Each map is composed of radiative flux trends which correspond the strongest 10% trends in the PDO index, averaged for each CMIP6 model. Multi-model median is computed among the maps obtained from 52 CMIP6 piControl simulations. Hatched regions represent areas where the Mann-Whitney-U test is passed at the 0.05 confidence level, i.e. differences between the distributions built from individual models for the PDO↑ and PDO↓ periods at that grid box are not statistically significant. Black boxes on the last map are those, over which we compute aggregated time series.

232 follow each other closely but with opposite sign, suggesting that changes in $F_{S,cs}^\downarrow$ are
 233 primarily mediated by changes in $A_{atm,cs}$. The absorbed clear-sky shortwave radiation at
 234 the surface ($F_{S,cs}^\downarrow$ also resembles the $F_{S,cs}^\downarrow$ and $A_{atm,cs}$ for most ocean areas except for
 235 the parts where sea ice plays a role. The clear-sky $F_{T,cs}^\uparrow$ in the Arctic regions increases
 236 with PDO↑, which is associated with less reflectivity in the system, likely due to the
 237 decreased sea ice area during a warm PDO (Simon et al., 2022).

238 This surface albedo effect is also evident in the all-sky patterns. The difference in
 239 the all-sky A_{atm} and clear-sky $A_{atm,cs}$ implies that increased absorption in cloudy con-
 240 ditions due to multiple scattering is significant for regions like the North Pacific.

241 CREs at the surface and TOA, associated with the different PDO phases, also yield
 242 identical patterns and similar magnitudes to F_S^\downarrow , F_T^\uparrow and F_S^\uparrow , with the exception of the
 243 Arctic. The increase of F_S^\downarrow , respectively CRE_S (CRE becomes less negative), in the warm
 244 North Pacific pool and the decrease in the cold pool (CRE becomes more negative, i.e.
 245 more clouds) further serve to enhance the SST anomalies associated with PDO. An in-
 246 teresting feature is the shift from enhanced F_S^\downarrow , F_T^\uparrow and F_S^\uparrow in the warm region during
 247 a PDO↑ and the opposite sign trends over North America.

248 We assess the uncertainty of the presented results on a grid box level in two ways:
 249 we test whether the samples assembled upon results from individual models for PDO↑
 250 (first sample) and PDO↓ (second sample) are part of the same distribution using the Mann-

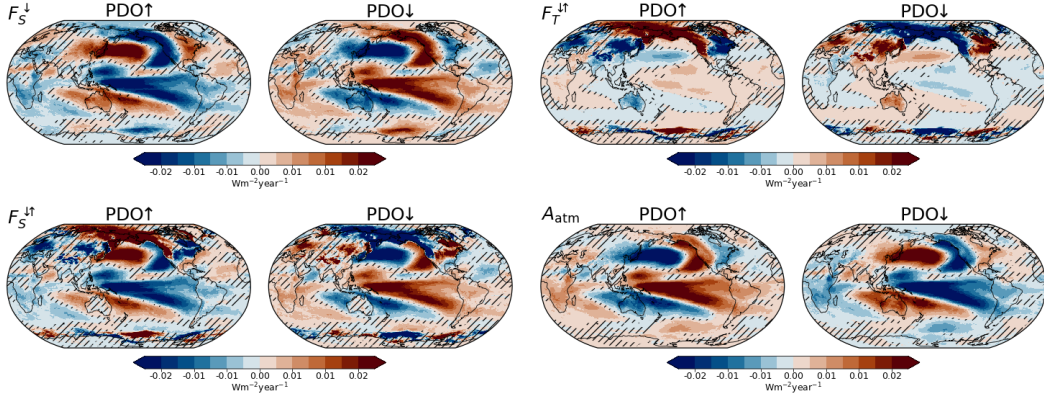


Figure 3. Same as Figure 2 but for the clear-sky fluxes.

251 Whitney-U test (Mann & Whitney, 1947); we also compute the spread among models
 252 (difference between the 90th percentile and 10th percentile values) for each grid box. De-
 253 pending on variable, the Mann-Whitney-U test is passed on the 0.05 level in 27-39% of
 254 grid boxes (34% for F_S^{\downarrow}), i.e. for these grid boxes there is no statistically significant dif-
 255 ference between periods of strongest negative or positive changes in the PDO index. These
 256 regions are hatched in Figures 2 and 3. The CMIP6 multi-model spread across grid boxes
 257 is on average $0.12\text{Wm}^{-2}\text{year}^{-1}$ for the all-sky fluxes and CRE (apart from A_{atm}) and
 258 on average $0.02\text{Wm}^{-2}\text{year}^{-1}$ for the clear-sky fluxes and all-sky A_{atm} (given are median
 259 values across grid boxes representative for all variables). Model spread also depends on
 260 the region and is highest in regions where the trend values are the highest. In relative
 261 units, the spread in clear-sky fluxes across models is higher in clear-sky as compared to
 262 all-sky, which was also highlighted in Chtirkova et al. (2022).

263 The differences among models with regard to PDO and its relation to shortwave
 264 fluxes may be illustrated by inspecting the model specific correlations between the PDO
 265 index annual mean time series and regionally averaged annual mean shortwave flux time
 266 series, even though they cannot be directly related to the decadal scales discussed above.
 267 Corresponding Pearson correlation coefficients are given in Table 1. We choose the four
 268 regions (see last map on Figure 2): North America and Europe, where our trend maps
 269 show a negative correlation for the all-sky fluxes (apart from A_{atm}) and India and In-
 270 dochinese Peninsula and Australia where the maps show a positive relationship. For F_S^{\downarrow} ,
 271 F_T^{\uparrow} and F_S^{\uparrow} , almost all models agree on the sign of the relationship in these regions. Ex-
 272 ceptions include EC-Earth3, INM-CM4-8, INM-CM5-0 and NorCPM1. Exceptions for
 273 A_{atm} , occur more often but trend patterns are also different for A_{atm} as compared to F_S^{\downarrow}
 274 and the choice of regions is not optimal for A_{atm} . We also highlight the models which
 275 show the strongest correlation coefficients between the PDO index and shortwave fluxes
 276 in North America, India and Australia: CESM2-FV2, CESM2-WACCM-FV2, CMCC-
 277 CM2-SR5, CMCC-ESM2, GFDL-ESM4, GISS-E2-1-G (p5), ICON-ESM-LR and MIROC6
 278 (given are models showing a correlation coefficient above 0.5 for at least one region and
 279 variable). The weaker correlations for Europe are expected due to its larger distance from
 280 the Pacific Ocean and other causes for variability there but models still agree on the sign
 281 of the relationship.

282 Going back to trend magnitudes and Figures 2 and 3, we mark as important that
 283 even though trend magnitudes are given in absolute units, they are strongly dependent
 284 on model and percentile of the PDO index trends over which we select periods. Trend
 285 magnitudes are on average 23-28% stronger (depending on variable) when increasing the
 286 percentile range from 90-10 (as shown on Figures 2 and 3) to 95-5. This happens for a

Table 1. Pearson correlation coefficients between the annual mean PDO index and all-sky shortwave components of the energy balance: downwelling at surface (F_S^\downarrow), net at TOA (F_T^\uparrow), net at surface (F_S^\uparrow), and absorbed by the atmosphere (A_{atm}). The SW components are taken as spatially aggregated annual-mean time series for four different regions (drawn on Figure 2). Bold font indicates absolute value of the correlation coefficient larger than or equal to 0.5. Correlation coefficients are calculated over the entire piControl simulations, which yields a different number of years for each model.

| Model | North America | | | | Europe | | | | India and Indochinese Peninsula | | | | Australia | | | |
|------------------|------------------|----------------|----------------|-------------|------------------|----------------|----------------|-----------|---------------------------------|----------------|----------------|--------------|------------------|----------------|----------------|--------------|
| | F_S^\downarrow | F_T^\uparrow | F_S^\uparrow | A_{atm} | F_S^\downarrow | F_T^\uparrow | F_S^\uparrow | A_{atm} | F_S^\downarrow | F_T^\uparrow | F_S^\uparrow | A_{atm} | F_S^\downarrow | F_T^\uparrow | F_S^\uparrow | A_{atm} |
| ACCESS-CM2 | -0.38 | -0.35 | -0.36 | 0.25 | -0.16 | -0.20 | -0.20 | 0.03 | 0.22 | 0.23 | 0.22 | -0.06 | 0.18 | 0.19 | 0.19 | -0.15 |
| ACCESS-ESM1-5 | -0.42 | -0.38 | -0.40 | 0.44 | -0.21 | -0.22 | -0.22 | 0.16 | 0.27 | 0.29 | 0.26 | 0.03 | 0.32 | 0.31 | 0.31 | -0.28 |
| AWI-CM-1-1-MR | -0.30 | -0.27 | -0.28 | 0.24 | -0.16 | -0.17 | -0.17 | 0.12 | 0.07 | 0.06 | 0.05 | 0.04 | 0.27 | 0.27 | 0.27 | -0.25 |
| BCC-CSM2-MR | -0.26 | -0.26 | -0.27 | 0.26 | -0.15 | -0.16 | -0.16 | 0.13 | 0.11 | 0.13 | 0.11 | 0.07 | 0.19 | 0.18 | 0.18 | -0.14 |
| BCC-ESM1 | -0.33 | -0.33 | -0.35 | 0.34 | -0.10 | -0.12 | -0.12 | 0.02 | 0.00 | 0.02 | 0.01 | 0.14 | 0.12 | 0.12 | 0.12 | -0.09 |
| CAS-ESM2-0 | -0.49 | -0.46 | 0.03 | -0.46 | -0.22 | -0.24 | 0.02 | -0.24 | 0.31 | 0.34 | -0.01 | 0.34 | 0.35 | 0.36 | -0.03 | 0.36 |
| CESM2 | -0.43 | -0.22 | -0.27 | 0.41 | -0.19 | -0.22 | -0.23 | 0.19 | 0.38 | 0.41 | 0.37 | 0.07 | 0.41 | 0.41 | 0.34 | -0.10 |
| CESM2-FV2 | -0.52 | -0.48 | -0.49 | 0.37 | -0.16 | -0.18 | -0.18 | 0.13 | 0.44 | 0.44 | 0.43 | -0.22 | 0.49 | 0.48 | 0.47 | -0.41 |
| CESM2-WACCM | -0.47 | -0.25 | -0.30 | 0.46 | -0.12 | -0.13 | -0.15 | 0.19 | 0.37 | 0.39 | 0.36 | -0.02 | 0.41 | 0.40 | 0.35 | -0.15 |
| CESM2-WACCM-FV2 | -0.59 | -0.50 | -0.52 | 0.50 | -0.19 | -0.19 | -0.21 | 0.23 | 0.55 | 0.55 | 0.54 | -0.32 | 0.48 | 0.49 | 0.44 | -0.20 |
| CIESM | -0.47 | -0.28 | -0.32 | 0.43 | -0.10 | -0.10 | -0.10 | 0.09 | 0.22 | 0.25 | 0.22 | -0.01 | 0.29 | 0.30 | 0.29 | -0.24 |
| CMCC-CM2-SR5 | -0.47 | -0.32 | -0.35 | 0.44 | -0.20 | -0.25 | -0.25 | 0.18 | 0.46 | 0.47 | 0.44 | -0.13 | 0.52 | 0.50 | 0.51 | -0.50 |
| CMCC-ESM2 | -0.51 | -0.37 | -0.40 | 0.44 | -0.26 | -0.30 | -0.31 | 0.25 | 0.54 | 0.54 | 0.52 | -0.23 | 0.58 | 0.57 | 0.58 | -0.56 |
| CNRM-CM6-1 | -0.11 | -0.18 | -0.19 | 0.10 | -0.11 | -0.18 | -0.18 | 0.04 | 0.16 | 0.18 | 0.17 | -0.03 | 0.17 | 0.18 | 0.17 | -0.14 |
| CNRM-ESM2-1 | -0.11 | -0.12 | -0.13 | 0.16 | -0.11 | -0.17 | -0.16 | 0.06 | 0.22 | 0.25 | 0.23 | -0.05 | 0.15 | 0.16 | 0.15 | -0.13 |
| CanESM5 (p1) | -0.28 | -0.14 | -0.17 | 0.16 | -0.22 | -0.22 | -0.22 | 0.14 | 0.29 | 0.33 | 0.29 | -0.06 | 0.35 | 0.36 | 0.35 | -0.33 |
| CanESM5 (p2) | -0.23 | -0.14 | -0.15 | 0.09 | -0.21 | -0.24 | -0.23 | 0.12 | 0.31 | 0.34 | 0.31 | -0.08 | 0.35 | 0.36 | 0.35 | -0.33 |
| CanESM5-CanOE | -0.25 | -0.17 | -0.18 | 0.12 | -0.20 | -0.24 | -0.23 | 0.11 | 0.33 | 0.36 | 0.32 | -0.11 | 0.37 | 0.37 | 0.37 | -0.36 |
| E3SM-1-0 | -0.42 | -0.29 | -0.33 | 0.43 | -0.12 | -0.13 | -0.14 | 0.17 | 0.15 | 0.15 | 0.15 | -0.05 | 0.13 | 0.15 | 0.13 | -0.06 |
| EC-Earth3 | -0.22 | -0.24 | -0.24 | 0.15 | 0.05 | -0.17 | -0.15 | -0.07 | 0.27 | 0.27 | 0.27 | -0.21 | 0.17 | 0.17 | 0.17 | -0.15 |
| EC-Earth3-CC | -0.38 | -0.26 | -0.29 | 0.35 | -0.08 | -0.23 | -0.23 | 0.14 | 0.34 | 0.34 | 0.33 | -0.21 | 0.28 | 0.26 | 0.26 | -0.24 |
| FGOALS-f3-L | -0.31 | -0.19 | -0.22 | 0.29 | -0.21 | -0.26 | -0.25 | 0.10 | 0.17 | 0.20 | 0.16 | 0.08 | 0.04 | 0.06 | 0.05 | 0.04 |
| FGOALS-g3 | -0.18 | -0.25 | -0.26 | 0.25 | -0.20 | -0.31 | -0.30 | 0.19 | 0.21 | 0.22 | 0.21 | -0.06 | 0.24 | 0.26 | 0.24 | -0.16 |
| GFDL-CM4 | -0.38 | -0.29 | -0.31 | 0.29 | -0.14 | -0.18 | -0.18 | 0.05 | 0.38 | 0.43 | 0.38 | 0.18 | 0.31 | 0.33 | 0.32 | -0.23 |
| GFDL-ESM4 | -0.55 | -0.50 | -0.52 | 0.45 | -0.19 | -0.18 | -0.19 | 0.13 | 0.31 | 0.35 | 0.29 | 0.24 | 0.42 | 0.42 | 0.39 | -0.08 |
| GISS-E2-1-G (f1) | -0.24 | -0.32 | -0.31 | 0.14 | -0.31 | -0.32 | -0.32 | 0.17 | 0.46 | 0.48 | 0.46 | 0.05 | 0.23 | 0.25 | 0.23 | -0.14 |
| GISS-E2-1-G (f2) | -0.28 | -0.33 | -0.33 | 0.24 | -0.28 | -0.31 | -0.31 | 0.10 | 0.41 | 0.44 | 0.41 | 0.04 | 0.26 | 0.27 | 0.25 | -0.16 |
| GISS-E2-1-G (p3) | -0.28 | -0.32 | -0.33 | 0.36 | -0.41 | -0.42 | -0.42 | 0.28 | 0.39 | 0.43 | 0.39 | 0.14 | 0.23 | 0.25 | 0.22 | -0.12 |
| GISS-E2-1-G (p5) | -0.37 | -0.42 | -0.43 | 0.40 | -0.40 | -0.41 | -0.42 | 0.23 | 0.51 | 0.56 | 0.51 | 0.30 | 0.24 | 0.26 | 0.23 | -0.07 |
| GISS-E2-1-H (f1) | -0.27 | -0.28 | -0.29 | 0.23 | -0.18 | -0.21 | -0.20 | 0.04 | 0.37 | 0.39 | 0.37 | -0.01 | 0.18 | 0.18 | 0.18 | -0.13 |
| GISS-E2-1-H (f2) | -0.18 | -0.19 | -0.19 | 0.12 | -0.15 | -0.16 | -0.15 | 0.07 | 0.34 | 0.35 | 0.34 | -0.03 | 0.20 | 0.21 | 0.20 | -0.12 |
| GISS-E2-1-H (p3) | -0.19 | -0.17 | -0.20 | 0.31 | -0.26 | -0.26 | -0.26 | 0.19 | 0.28 | 0.30 | 0.28 | 0.05 | 0.17 | 0.18 | 0.17 | -0.10 |
| HadGEM3-GC31-LL | -0.42 | -0.36 | -0.38 | 0.35 | -0.21 | -0.21 | -0.23 | 0.20 | 0.32 | 0.34 | 0.32 | -0.01 | 0.26 | 0.30 | 0.27 | -0.14 |
| HadGEM3-GC31-MM | -0.32 | -0.22 | -0.25 | 0.25 | -0.16 | -0.19 | -0.20 | 0.14 | 0.34 | 0.34 | 0.34 | -0.14 | 0.10 | 0.15 | 0.10 | -0.01 |
| ICON-ESM-LR | -0.57 | -0.59 | -0.58 | 0.42 | -0.19 | -0.22 | -0.21 | 0.12 | 0.59 | 0.58 | 0.59 | -0.51 | 0.47 | 0.46 | 0.47 | -0.48 |
| INM-CM4-8 | -0.26 | -0.29 | -0.28 | 0.07 | -0.08 | -0.06 | -0.06 | 0.04 | -0.06 | -0.06 | -0.06 | 0.08 | 0.27 | 0.27 | 0.27 | -0.19 |
| INM-CM5-0 | -0.19 | -0.25 | -0.24 | 0.05 | -0.10 | -0.15 | -0.14 | 0.04 | -0.15 | -0.14 | -0.15 | 0.21 | 0.02 | 0.01 | 0.02 | -0.04 |
| IPSL-CM6A-LR | -0.29 | -0.30 | -0.29 | 0.16 | -0.14 | -0.18 | -0.18 | 0.07 | 0.02 | 0.05 | 0.02 | 0.06 | 0.28 | 0.28 | 0.28 | -0.28 |
| KACE-1-0-G | -0.33 | -0.17 | -0.22 | 0.34 | -0.13 | -0.13 | -0.15 | 0.21 | 0.23 | 0.24 | 0.23 | -0.03 | 0.12 | 0.17 | 0.12 | 0.00 |
| MIROC-ES2H | -0.44 | -0.33 | -0.37 | 0.45 | -0.17 | -0.20 | -0.20 | 0.14 | 0.39 | 0.44 | 0.39 | 0.28 | 0.32 | 0.33 | 0.33 | -0.27 |
| MIROC-ES2L | -0.42 | -0.35 | -0.41 | 0.49 | -0.14 | -0.15 | -0.16 | 0.16 | 0.30 | 0.41 | 0.31 | 0.46 | 0.20 | 0.20 | 0.21 | -0.19 |
| MIROC6 | -0.55 | -0.39 | -0.44 | 0.57 | -0.17 | -0.20 | -0.21 | 0.22 | 0.35 | 0.41 | 0.35 | 0.40 | 0.39 | 0.41 | 0.40 | -0.33 |
| MPI-ESM-1-2-HAM | -0.36 | -0.35 | -0.36 | 0.29 | -0.28 | -0.27 | -0.27 | 0.23 | 0.04 | 0.06 | 0.02 | 0.16 | 0.27 | 0.27 | 0.27 | -0.25 |
| MPI-ESM1-2-HR | -0.27 | -0.23 | -0.24 | 0.19 | -0.21 | -0.22 | -0.22 | 0.10 | 0.14 | 0.16 | 0.11 | 0.14 | 0.25 | 0.28 | 0.26 | -0.18 |
| MPI-ESM1-2-LR | -0.42 | -0.41 | -0.41 | 0.33 | -0.24 | -0.25 | -0.25 | 0.22 | 0.15 | 0.17 | 0.13 | 0.07 | 0.27 | 0.28 | 0.27 | -0.22 |
| MRI-ESM2-0 | -0.35 | -0.20 | -0.24 | 0.33 | -0.07 | -0.10 | -0.09 | 0.02 | 0.30 | 0.35 | 0.31 | 0.03 | 0.18 | 0.20 | 0.18 | -0.08 |
| NESM3 | -0.10 | -0.17 | -0.12 | -0.17 | -0.10 | -0.12 | -0.10 | -0.03 | 0.14 | 0.13 | 0.14 | -0.13 | 0.11 | 0.10 | 0.11 | -0.11 |
| NorCPM1 (r1) | -0.06 | 0.02 | 0.00 | 0.10 | -0.24 | -0.25 | -0.25 | 0.15 | 0.25 | 0.27 | 0.24 | 0.13 | 0.25 | 0.25 | 0.24 | -0.18 |
| NorCPM1 (r2) | -0.20 | -0.17 | -0.18 | 0.20 | -0.29 | -0.30 | -0.29 | 0.10 | 0.28 | 0.29 | 0.27 | 0.08 | 0.32 | 0.34 | 0.32 | -0.24 |
| NorCPM1 (r3) | -0.12 | -0.06 | -0.08 | 0.19 | -0.27 | -0.26 | -0.27 | 0.20 | 0.25 | 0.27 | 0.24 | 0.15 | 0.32 | 0.32 | 0.32 | -0.26 |
| SAM0-UNICON | -0.46 | -0.22 | -0.26 | 0.41 | -0.20 | -0.20 | -0.21 | 0.18 | 0.34 | 0.35 | 0.34 | -0.18 | 0.49 | 0.49 | 0.49 | -0.47 |
| UKESM1-0-LL | -0.43 | -0.41 | -0.44 | 0.48 | -0.19 | -0.22 | -0.24 | 0.29 | 0.27 | 0.28 | 0.27 | -0.09 | 0.34 | 0.37 | 0.36 | -0.29 |
| Median | -0.33 | -0.28 | -0.29 | 0.29 | -0.19 | -0.21 | -0.21 | 0.14 | 0.30 | 0.34 | 0.29 | 0.03 | 0.27 | 0.27 | 0.27 | -0.17 |

287 few reasons: (1) PDO trends across models differ and (2) PDO trends in the same model
 288 above the 90th percentile differ, (3) the atmospheric response to the same PDO trend
 289 across models might be different. Taking a smaller subset of PDO indices does not nec-
 290 essarily provide better statistics because of too much non-PDO related variability that
 291 is not averaged across many data points. To further quantify what fraction of the vari-
 292 ability is attributable to the PDO and what are the specific radiative anomalies related
 293 to its phases, we rely on results from simplified numerical experiments described in the
 294 following sections.

295 3.2 PDO fraction in variability

296 In our simplified ICON-A numerical setup, we would firstly like to give an estimate
 297 on what fraction of total shortwave flux variability can be attributed to the SST field
 298 and what fraction of that is attributable to the PDO pattern. To achieve this, we first

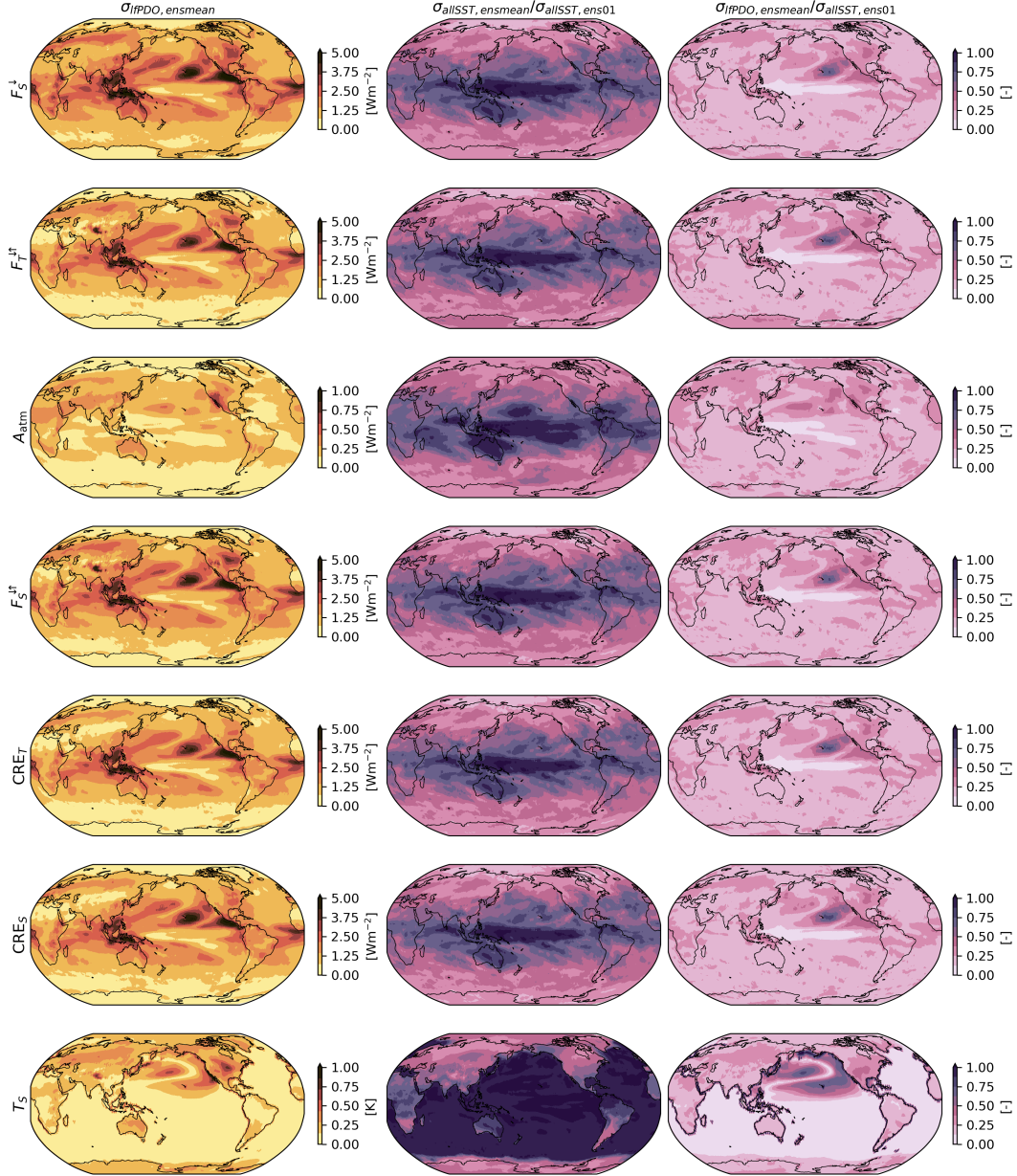


Figure 4. Standard deviation of the annual mean time series per grid box of the the 20-ensemble-member mean low frequency PDO experiment for different variables (first column), ratio between the standard deviation of the 20-ensemble-member mean in the all SST experiment and the standard deviation for the control run (second column) and ratio between the standard deviation of the 20-ensemble-member mean in the low-frequency PDO experiment and the control run (third column). The control run is one ensemble member of the all SST experiment.

299 need to separate atmosphere-only variability from SST-related atmosphere-ocean vari-
 300 ability. We do so by running 20 ensemble members with SSTs directly taken from the
 301 coupled run (“allSST”): one ensemble member of this experiment (our control run) should
 302 possess both atmosphere and coupled variability. The atmosphere-only variability should
 303 be averaged out in the ensemble mean time series (average time series across ensemble

members for each grid box) and the only remaining variability in the 95-year ensemble mean should be related to the prescribed time-varying SSTs, as they are the only time-evolving boundary condition in our “allSST” experimental setup.

Taking this idea further, annual mean time series averaged over the 20 ensemble members of the “lfpdo” experiment should retain only variability associated with the low frequency PDO variability. The standard deviation of the latter (computed upon the 95-year ensemble mean time series per grid box) is shown on Figure 4, first column. We also show results for the surface temperature T_S (last row on Figure 4) because they best illustrate the direct effect of the experimental setup. Testing for a different number of ensemble members, we find the resulting reduction of variability converges for around 10 ensemble members.

To gain an impression of the relative importance of SST variability in general and PDO variability in particular, we compute the differences relative to the control run of the standard deviations of the time series per grid box as: $\sigma_{\text{allSST,ensmean}}/\sigma_{\text{allSST,ens01}}$, where $\sigma_{\text{allSST,ensmean}}$ is the per grid box standard deviation of the ensemble mean time series (atmosphere-only variability is averaged out), and $\sigma_{\text{allSST,ens01}}$ is the per grid box standard deviation of one of the ensemble members (our control run; includes atmospheric variability; results are not sensitive to the choice of specific ensemble member). The ratio is shown on Figure 4, second column. We see that SST-related variability is responsible for almost all of total (atmosphere and ocean) variability in the tropical regions. The standard deviation for the ensemble mean is reduced in roughly half for the short-wave flux variables for continental regions like North America and Europe (on a grid box level). Looking into spatially averaged (aggregated) time series instead of individual grid boxes (i.e. taking the spatially averaged time series and computing its standard deviation instead of averaging the standard deviations of the time series per grid box), the resulting ratio $\sigma_{\text{allSST,ensmean}}/\sigma_{\text{allSST,ens01}}$ is 10-30% more (not shown), i.e. SSTs explain a larger fraction of variability for spatially averaged time series across regions than for individual grid boxes. This is not surprising because the influence of the SSTs over land usually occurs thorough the large-scale circulation, the effect of which is reduced at the grid box level from small-scale noise and this small-scale noise is already averaged out in the aggregated time series, yielding a smaller reduction in variability. For the aggregated time series in our regions of interest, we find that the ratio is 0.78 for F_S^\downarrow and 0.69 for F_T^\uparrow for North America, 0.53 for F_S^\downarrow and 0.54 for F_T^\uparrow for Europe and 0.74 for both F_S^\downarrow and F_T^\uparrow for India and Indochinese peninsula. The fraction of variability of CRE that can be related to the time evolving SSTs is 0.62 of the variability in the Northern Hemisphere (0.57 for North America, 0.45 for Europe and 0.67 for India and Indochinese peninsula).

The second step is to estimate how much of the total variability is related to the low-frequency PDO pattern. We do so by computing the ratio between the 20-ensemble-member mean in the “lfpdo” experiment and the control run: $\sigma_{\text{lfpdo,ensmean}}/\sigma_{\text{allSST,ens01}}$. The result (third column on Figure 4) is that the low frequency component of the PDO in our experimental setup is related to almost none of the variability in the tropics for the variables we investigate, it is also no or little related to the SST-related variability in Australia and South America. For the Northern Hemisphere aggregated time series, the PDO is related to a fraction of 0.37-0.44 (depending on the variable) of SST-related variability. For the shortwave radiative fluxes $\sigma_{\text{lfpdo,ensmean}}/\sigma_{\text{allSST,ens01}}$ this is 0.24-0.25 (depending on the variable) on average for individual grid boxes in the Northern Hemisphere. For spatially aggregated time series in the Northern Hemisphere, the fraction of total variability attributable to PDO is 0.33-0.35, for North America – 0.39-0.42, for Europe – 0.27-0.31, for India and Indochinese peninsula – 0.22-0.27. The fractions of variability presented in this section are indicative for the variability of annual mean time series and become larger for longer time scales, at which higher frequency atmospheric noise plays a smaller role (not shown).

357
358

3.3 Quantification of shortwave radiative flux anomalies associated with PDO phases

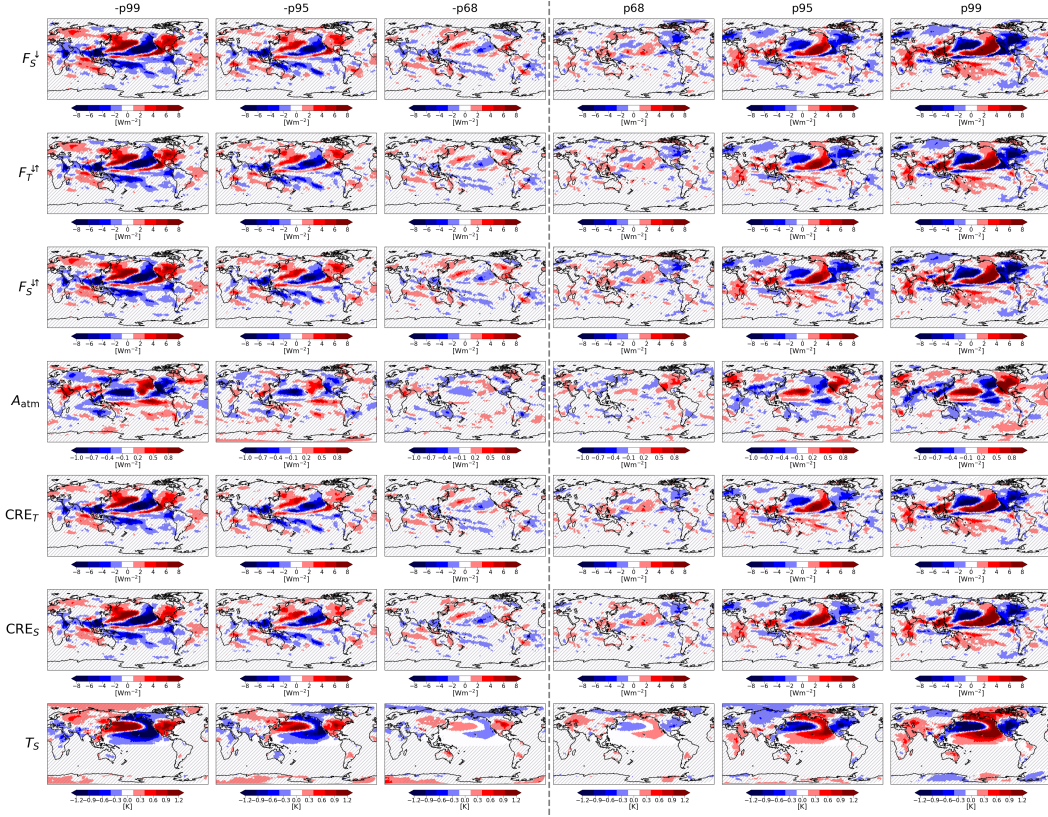


Figure 5. All-sky shortwave flux, cloud radiative effect and surface temperature anomalies computed for each “perpetual PDO” experiment ($\overline{PC}_1(t) \in [-2.58(-p99), -1.64(-p95), -0.44(-p68), 0.44(p68), 1.64(p95), 2.58(p99)]$) relative to the control run ($\overline{PC}_1(t) = 0$). Hatched regions represent areas where the Student-t test is passed at the 0.05 significance level, i.e. the null hypothesis of equal population means of the two samples (time series in experiment and control in individual grid boxes) cannot be rejected.

359 We remove the temporal element of the PDO evolution and use the “perpetual”
 360 PDO set of simulations to quantify the increase in each of the radiative fluxes as a func-
 361 tion of the PDO index value which is embroidered in the climatological SST field as anom-
 362 alies in space (exact SST anomalies are shown on Figure A3). Each simulation is conducted
 363 with a constant in time PDO index value; the index values are chosen as different per-
 364 centile of the distribution of all PDO index values obtained from the 500-year coupled
 365 simulation. By computing the difference between the mean time series of each exper-
 366 iment and the control run (neutral PDO), we obtain radiative flux anomalies per grid box
 367 which correspond to the different simulations (PDO indices). The spatial distribution
 368 of the radiative flux and surface temperature anomalies are shown on Figure 5. Com-
 369 paring the spatial patterns to the trends distribution obtained from CMIP6 (Figure 2)
 370 for F_S^{\downarrow} , F_T^{\uparrow} and F_S^{\uparrow} , we observe similarities in the Northern Hemisphere, including the
 371 North Pacific region, North America, Europe and Southern Asia. A prominent differ-
 372 ence observed in the Southern hemisphere is Australia. In the fully-coupled CMIP6 sim-
 373 ulations, where the PDO occurs in combination with other modes of ocean variability,
 374 Australia evolves in phase with South Asia. By contrast, in our simulations where the

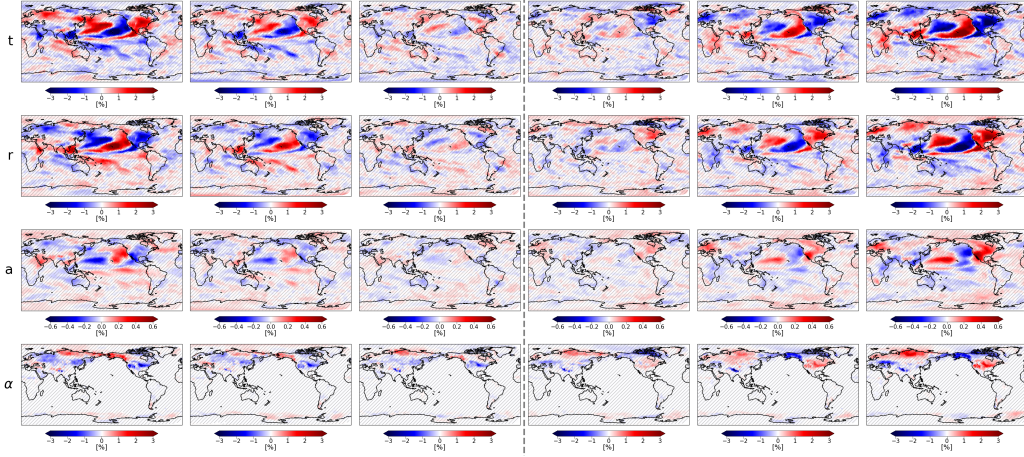


Figure 6. Same as Figure 5 but for anomalies in atmospheric transmittance, reflection, absorption and surface albedo.

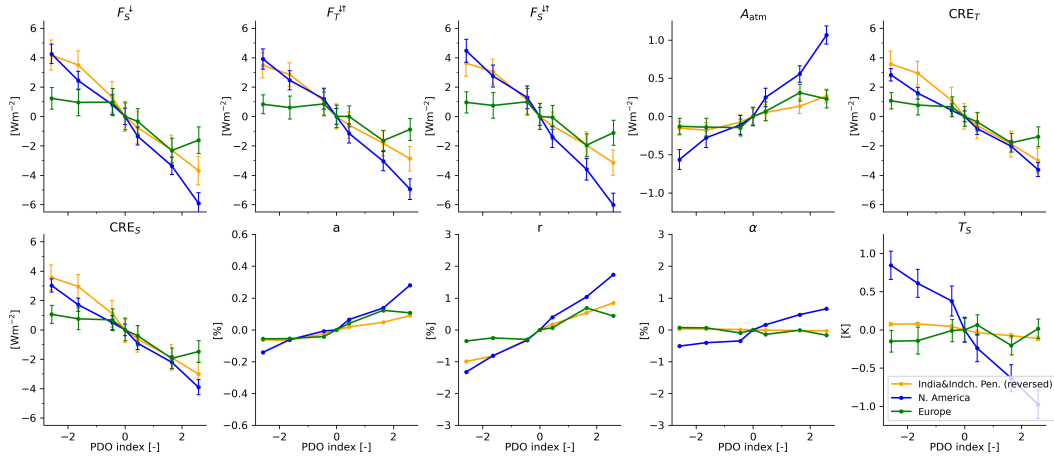


Figure 7. Scatter plots for different variables as a function of the PDO index value for regions denoted on Figure 2. The regional means for India and Indochinese peninsula are multiplied by -1 . Uncertainty ranges show the 95% confidence interval determined via t-statistics. Values on y-axis depend on the exact choice of region boundaries, which is arbitrary.

375 PDO exists in isolation, this connection between Australia and South Asia is broken. The
 376 differences between our ICON-A simulations and CMIP6 will be further addressed in the
 377 discussion.

378 Comparing the simulations that differ in the strength and sign of the PDO SST
 379 anomaly (the different columns on Figure 5), we observe prominent and statistically sig-
 380 nificant differences in the simulations that correspond to higher percentiles (95, 99). In
 381 the p68, -p68 experiments, where the spatial SST anomaly is not as strong, the patterns
 382 of the radiative flux response cover smaller areas that appear scattered, but the result-
 383 ing anomaly is of the same sign as in the simulations with stronger anomalies. We as-
 384 sess the statistical significance per grid box by performing Student t-test (Student, 1908)
 385 between the time series in the control run and the one in the corresponding experiments.
 386 Our null hypothesis that the two samples come from the same population is rejected in
 387 23-29% (depending on the radiative flux variable) of the boxes in the Northern Hemi-

388 sphere for the p95 simulation and in 40-42% for the p99 simulation. These include most
 389 of the North Pacific Ocean, North America, South India, the Indochinese Peninsula and
 390 East Africa, more pronounced in the Ethiopian Highlands. The null hypothesis cannot
 391 be rejected at the 0.05 level for most of Europe (depending on the variable and exper-
 392 iment), indicating that the atmosphere-only variability can easily mask the PDO signal
 393 in a statistical test.

394 Based on the anomalies that correspond to -p95 and p95 (second and fifth columns
 395 on Figure 5), the surface and TOA radiative flux anomalies reach up to $\pm 6 \text{ Wm}^{-2}$ for
 396 parts of North America, $\mp 3 \text{ Wm}^{-2}$ for India and $\pm 2 \text{ Wm}^{-2}$ for parts of Europe. These
 397 numbers represent per grid box anomalies associated with the PDO range of $[-1.64; 1.64]$
 398 in the 95-year mean where atmospheric noise is averaged out.

To draw a more general picture and exploit the connections and similarities between
 the radiative fluxes, we decompose the observed changes to changes in the optical prop-
 erties of the atmospheric column (transmittance, reflection and absorption) and changes
 in surface reflection (albedo) in relation to the PDO anomaly (our different simulations).
 To do so, we closely follow the decomposition described in Stephens et al. (2015) and Loeb
 et al. (2019), who use the upwelling and downwelling shortwave fluxes at TOA and at
 the surface: $F_T^\downarrow = S$ (downwelling shortwave at TOA), F_T^\uparrow , F_S^\downarrow , F_S^\uparrow . Exactly following
 Stephens et al. (2015), where further details may be found, we define the effective sur-
 face albedo α , the system transmittance T and the system reflectance R as:

$$\alpha = \frac{F_S^\uparrow}{F_S^\downarrow}, \quad (1)$$

$$R = \frac{F_T^\uparrow}{S} = r + \frac{tat}{1 - r\alpha}, \quad (2)$$

$$T = \frac{F_S^\downarrow}{S} = \frac{t}{1 - r\alpha}, \quad (3)$$

399 where t and r are the atmospheric transmissivity and reflection for a single beam, given
 400 the assumption that the atmosphere reflects and transmits equally in both upward and
 401 downward directions. The system reflectance R includes the reflected energy from the
 402 atmosphere rS plus the multiple scattering between the surface and atmosphere, it cor-
 403 responds to Earth’s planetary albedo (Stephens et al., 2015).

We can compute t and r from the T and R (and the radiative fluxes respectively)
 by:

$$t = T \frac{1 - \alpha R}{1 - \alpha^2 T^2} \quad (4)$$

$$r = R - t\alpha T \quad (5)$$

To better carve the energy partitioning, we express the atmospheric transmissivity t as:

$$t = 1 - a - r, \quad (6)$$

404 where $a = 1 - r - t$ is the fraction of the beam that is absorbed by the atmosphere.
 405 This gives a more clear separation on whether the excess energy that does not reach the
 406 surface goes into heating the atmosphere.

407 The spatial patterns of t , r , a and α are shown on Figure 6. It is evident that r closely
 408 resembles the patterns of changes in CRE (Figure 5), cloud cover, cloud liquid water and
 409 cloud ice content (not shown). a is similar to A_{atm} , as is to be expected, but their pat-
 410 tern does not closely follow the column integrated water vapour content (not shown),
 411 as clouds are also essential for atmospheric absorption (see section 3.1). The surface albedo
 412 α has its own unique pattern, which is enhanced when looking only at winter months
 413 (not shown), indicating that the changes are associated mainly with changes in snow cover.

414 There is an increase in α in North America during a positive PDO, in line with increased
 415 r in the region. Over Eurasia, the change in α is not symmetric for the positive and neg-
 416 ative PDO phases: the increase in during a positive PDO seems to extend South to around
 417 55°N , while during a negative phase, there is an increase in North Siberia (South to 60°N),
 418 and a decrease further South.

419 To draw whether the response of the large-scale radiative fluxes to the SST anomaly
 420 related to the PDO is linear or not, we take the anomalies of the spatially averaged time
 421 series in the regions discussed in the previous sections – North America, Europe and In-
 422 dia and Indochinese peninsula and plot the mean anomalies for each simulations as a func-
 423 tion of the “perpetual” PDO index driving the simulation. The anomalies are computed
 424 by aggregating the time series in the region, taking the time-mean across the last 95-years
 425 of the experiment run and subtracting the control run aggregated temporal mean. Re-
 426 sulting dependencies are shown on Figure 7 with the anomaly for India and Indochinese
 427 peninsula given with a negative sign to match the direction of the other curves. In the
 428 range of PDO indices we work in, the response of the radiative fluxes is mostly linear,
 429 even though there is asymmetry around zero for some regions and variables. For the ag-
 430 gregated time series in North America and India and Indochinese peninsula, the anomaly
 431 is about $\pm 4 \text{ Wm}^{-2}$ for PDO index values of -2.58, 2.58 (-p99, p99 in the ICON-ESM-
 432 LR piControl distribution) and about about $\pm 1 \text{ Wm}^{-2}$ for Europe. These values depend
 433 on the exact choice of the regions, which is only done for illustrative purposes and is ar-
 434 bitrary.

435 Results for Europe are indistinguishable from the control run, given the 95% con-
 436 fidence interval of the uncertainty of the mean, which is also evident from the statisti-
 437 cal tests performed per grid box (Figure 5). However, the confidence intervals do not over-
 438 lap for the highest and lowest PDO values, showing a distinct and statistically signif-
 439 icant difference between the positive and negative values. The increase of both a and r
 440 from negative to positive PDO values, shows that they both contribute to the reduction
 441 F_S^\downarrow with the contribution of r being much larger. This is also evident when comparing
 442 the net radiative anomalies at the surface and TOA with F_T^\downarrow being always slightly smaller
 443 than F_S^\downarrow , implying that the increased atmospheric absorption slightly offsets the reduc-
 444 tion in F_S^\downarrow for a positive PDO phase. Unlike the radiative fluxes, the surface temper-
 445 ature, T_S , dependence is different in North America and Europe – the anomaly is neg-
 446 ative in North America and small but positive in Europe, which is also evident in the
 447 patterns on Figure 5.

Lastly, we assess the relative contributions of t , a and α to changes in F_S^\downarrow for the
 different PDO anomalies (simulations). We do so by expressing F_S^\downarrow as:

$$F_S^\downarrow = \frac{1 - r - a}{1 - r\alpha} S \quad (7)$$

Since S in our case does not have any inter-annual variability and by also omitting co-
 variance terms between δr , δa and $\delta\alpha$, we can approximate the change in F_S^\downarrow as:

$$\begin{aligned} \frac{\delta F_S^\downarrow}{S} &\approx \frac{-\delta a - \delta r}{1 - r\alpha} - \frac{(1 - r - a)(-r\delta\alpha - \alpha\delta r)}{(1 - r\alpha)^2} \\ &= \delta r \left(-\frac{1}{1 - r\alpha} - \frac{-\alpha(1 - r - a)}{(1 - r\alpha)^2} \right) + \delta a \left(\frac{-1}{1 - r\alpha} \right) \\ &\quad + \delta\alpha \left(\frac{(1 - r - a)(-r)}{(1 - r\alpha)^2} \right) \\ &= k_1\delta r + k_2\delta a + k_3\delta\alpha. \end{aligned} \quad (8)$$

448 The linear equation above allows us to attribute the changes in downwelling solar radi-
 449 ation δF_S^\downarrow to changes in the atmospheric and surface properties: δr , δa and $\delta\alpha$. A sim-
 450 ilar expression can also be obtained for the net fluxes at the surface and TOA but for
 451 this we limit ourselves only to downwelling surface radiation.

452 Taking the relative contributions as $\delta a S / \delta F_S^\downarrow$, $\delta r S / \delta F_S^\downarrow$ and $\delta \alpha S / \delta F_S^\downarrow$, we find that
 453 for the individual regions they are approximately constant for the different PDO index
 454 values (i.e. relative contributions of the different terms do not change with the PDO value),
 455 especially the higher ones, where δF_S^\downarrow is more distinct. The first thing we highlight is that
 456 the relative contributions depend on the region. For the ocean regions, where α is es-
 457 sentially constant, we note the following: in the Tropical extension of the PDO, almost
 458 all of the change in F_S^\downarrow comes from changes in the reflectivity of the atmosphere δr ; the
 459 same is true for the West part of the PDO region (cold region during a positive PDO
 460 phase) with only 2-3% of the changes in F_S^\downarrow being attributable to δa ; in the East part
 461 of the PDO (warm region during a positive phase), 86% of the changes in F_S^\downarrow are attributable
 462 to δr and around 14% to δa . Over India and Indochinese peninsula, 91% of the changes
 463 are attributable to δr and around 9% to δa . In the North American region, 93% of the
 464 changes can be attributed to δr , 13% – to δa , and 6% are offset by $\delta \alpha$, which dampens
 465 the reduction in F_S^\downarrow by increased snow cover during the positive PDO phase and the other
 466 way around for the negative phase. For Europe (excluding Scandinavia), the increase in
 467 r and a , and a reduction in α , all contribute to a reduction in F_S^\downarrow by 80%, 17% and 3%
 468 respectively. All percentages given are average contributions of the terms for the -p99,
 469 -p95, p95 and p99 simulations. The residual contributions of the covariance terms are
 470 less than 0.1% for all regions and experiments investigated.

471 4 Discussion

472 The discussion section is structured as follows: in the first part we compare results
 473 from our “perpetual” PDO ICON-A simulations to the coupled ICON-ESM-LR and CMIP6
 474 multi-model median to carve out differences that are due to coupling and differences be-
 475 tween ICON and the median across CMIP6 models. In the second part, we compare the
 476 PDO index amplitudes within ICON and observations, namely ERSST V5 (Huang et
 477 al., 2017).

478 Comparing the patterns between Figures 2 (CMIP6) and 5 (ICON-A), we observe
 479 differences in the shortwave radiative fluxes in the Southern Hemisphere, Australia, South
 480 America, the Arab peninsula and Sahara, Atlantic ocean and the Arctic. The radiative
 481 flux patterns for Australia, South Pacific, and South America are evident in both CMIP6
 482 multi-model median (Figure 2) and ICON-ESM-LR (Figure B1), implying that they re-
 483 sult from the coupling or a large-scale process related to the PDO that is not included
 484 in our experimental setup rather than differences between the ICON model and CMIP6.
 485 This suggests that the mechanisms responsible for Australian and South American ra-
 486 diative flux anomalies do not depend only on the PDO as a horseshoe phenomenon in
 487 the North Pacific, but on its basin-wide manifestation – IPO, which does not exist in that
 488 form in our “PDO only” simulations. Furthermore, the radiative fluxes in the South Pa-
 489 cific appear to be affected in a similar (but weaker) way as in CMIP6, which in a cou-
 490 pled simulation would have an effect on the SSTs and the dynamics thereafter. This change
 491 in the shortwave radiative fluxes (including unforced dimming and brightening) might
 492 be one of the mechanisms through which Northern extratropics communicate with South-
 493 ern hemisphere and PDO influences the SPDO and they combine into IPO.

494 The dimming above the Atlantic during PDO \uparrow that is evident in CMIP6 and ICON-
 495 ESM-LR (Figure B1) but not in our ICON-A (Figure 5) simulations implies that it ei-
 496 ther arises from the interaction between the atmosphere and ocean or there are other
 497 processes, independent from the North Pacific horseshoe pattern, that are related to the
 498 PDO. A mechanism that we propose is that the North Atlantic dimming in the coupled
 499 models might arise from the ocean transport (by surface currents like the Gulf stream)
 500 of cold waters from the East coast of North America into the ocean interior. The East
 501 coast is influenced by PDO-related dimming that is also evident in our atmosphere-only
 502 ICON-A simulations. This gives a hypothetical example of a communication mechanism
 503 between the North Pacific and North Atlantic oceans through surface shortwave fluxes.

504 The difference in the region of the Mediterranean Sea, Arab peninsula and Sahara:
 505 dimming in CMIP6 multi-model median and no-specific response or weak brightening
 506 in our ICON-A (Figure 5) simulations are also evident between the CMIP6 multi-model
 507 median (Figure 2) and ICON-ESM-LR (Figure B1), which implies that they are due to
 508 differences in the specific model response of ICON.

509 We also highlight that the correlation coefficients between ICON-ESM-LR and the
 510 shortwave fluxes are higher as compared to the majority of CMIP6 models, but such high
 511 correlation coefficients are also evident in model families such as CESM2, CMCC, GFDL
 512 and MIROC (Table 1). This stronger relationship is also evident in the stronger trend
 513 magnitudes in ICON-ESM-LR (Figure B1) as compared to CMIP6 multi-model median
 514 (Figure 2). It is also related to the large inter-model spread in the trend magnitudes es-
 515 timated in section 3.1. Whether the differences among models are due to a weaker SST
 516 anomaly or a different atmospheric response requires further investigation.

517 We next compare the PDO that we derived from ICON-ESM-LR to the PDO time
 518 series computed with the same method upon the ERSST-v5 reconstructed SST data (Huang
 519 et al., 2017) that covers the period 1920-2015 on a 2° grid with a monthly resolution. We
 520 decrease the imprint of global warming on the observational SST field by subtracting the
 521 global annual mean SST anomaly from each grid box. Extracting the first eigenvector
 522 (that corresponds to the PDO horseshoe) from the deseasonalized monthly anomalies
 523 in the observations, yields the historical PDO time series. The variance fraction explained
 524 by this principal component is 17%, in comparison for ICON-ESM-LR, the variance frac-
 525 tion is 25% (based on the ratio between the first eigenvalue divided by the sum of all eigen-
 526 values). To account for differences in the variance fraction, the principal component time
 527 series are usually normalized by their eigenvalues, which relates the magnitude of the spa-
 528 tial pattern (EOF) and the temporal variability (PC). We then compare the 95th per-
 529 centiles of the resulting distributions of PDO index values, that are 1.64 for ICON-ESM-
 530 LR and 1.58 for ERSST-v5, yielding a slightly stronger PDO amplitudes in ICON-ESM-
 531 LR as compared to ERSST-v5. The differences in variance fraction also imply that the
 532 observational SST field contains much more “noise” on top of the idealized PDO evo-
 533 lution that we analyse in this study. The pattern correlation for PDO between the ICON-
 534 ESM-LR and ERSST-v5 is 0.85 (computed on the ICON grid), typical for CMIP model
 535 ranges of 0.8-0.9 (Newman et al., 2016).

536 One might pose the question on why we use SSTs from the coupled piControl run
 537 instead of directly taking them from observations. The reasons for this are the follow-
 538 ing: (1) the piControl simulation is not contaminated by global warming and climate change;
 539 (2) we can build better statistics and derive a cleaner eigenvector from 500 years of data
 540 as compared to the shorter observational period; (3) the atmospheric dynamics within
 541 the model is aligned with the SSTs, which might be of relevance because SST patterns
 542 are a combination of atmospheric and oceanic processes and having a numerical mismatch
 543 between the atmosphere and SSTs might compromise a study that focuses solely on in-
 544 ternal variability. Given the comparison to observed SSTs above, we do not have indi-
 545 cations of significant biases in the PDO pattern selected for our experiments.

546 5 Summary

547 The present study targets the role of one specific mode of ocean variability – the
 548 PDO, in the variability of the shortwave flux components within Earth’s energy balance:
 549 F_S^\downarrow , F_T^\uparrow , F_S^\uparrow , A_{atm} , CRE_S , CRE_T . First, we look at them through the lens of the PDO
 550 in coupled simulations, i.e. the PDO as it is diagnosed via the PDO index in CMIP6 pi-
 551 Control simulations, where the it is naturally co-occurring with other modes of variabil-
 552 ity, notably ENSO and the SPDO. Seen through this PDO lens, the all-sky components
 553 of F_S^\downarrow , F_T^\uparrow , F_S^\uparrow , CRE_S , CRE_T show remarkably similar patterns associated with the PDO,
 554 highlighting the redistribution of clouds in sync with the PDO in the coupled system.

555 On the other hand, changes of all-sky A_{atm} and the clear-sky components in relation-
 556 ship to the PDO show different patterns that reflect the redistribution of shortwave absor-
 557 bers in the atmosphere (mainly water vapour) and changes in effective surface albedo
 558 in response to PDO.

559 Adjusting the PDO lens to focus, by experiment design, exclusively on the North
 560 Pacific horseshoe and its year-to-year variability, we ask the question what is the frac-
 561 tion of total year-to-year variability that can be related to the PDO. To do so, we run
 562 ensemble atmosphere-only simulations with ICON-A (each with length 100 years) that
 563 allow us to average out atmosphere-only variability for an all SST (“allSST”) case and
 564 a low frequency PDO case (“lfPDO”). The “allSST” experiment contains the SSTs di-
 565 rectly taken from the coupled piControl run of ICON-ESM-LR, while the “lfPDO” ex-
 566 periment contains only the low-frequency component of the PDO time series projected
 567 on the SST field. We show that SST-related variability (including ENSO) is related to
 568 almost all variability of shortwave fluxes in the tropics and about half of the variabil-
 569 ity in the extratropics. The PDO alone (constrained to the North Pacific) is related to
 570 almost none of the variability in the tropics and around 20-40% of variability of the short-
 571 wave fluxes over the Northern Hemispheric continents. We also show that over land, SST-
 572 related variability is more evident in spatially averaged (aggregated) time series as com-
 573 pared to individual grid boxes. This is because the SSTs impact on large-scale dynam-
 574 ics is prone to be blurred by small-scale noise.

575 Keeping the idealized spatial form of the PDO lens but now idealizing also the tem-
 576 poral manifestation, we carry out a set of “perpetual” PDO simulations, each correspond-
 577 ing to a different PDO anomaly in space. When comparing the geographical patterns
 578 of shortwave flux anomalies we obtain this way to geographical patterns of trends within
 579 the CMIP6 data set, we find overall agreement in the Northern Hemisphere. We show
 580 that the mean anomalies on a grid box level for North America reach up to $\pm 6 \text{ Wm}^{-2}$;
 581 for India and Indochinese peninsula – up to $\mp 3 \text{ Wm}^{-2}$; and for Europe – up to $\pm 2 \text{ Wm}^{-2}$.
 582 Numbers represent anomalies associated with the PDO range of $[-1.64; 1.64]$ (-p95 and
 583 p95) taken from the temporal mean of each 100-year simulation, where atmospheric vari-
 584 ability is averaged out.

585 Focusing on changes in F_S^\downarrow , induced by the PDO, we find that the relative contri-
 586 butions of changes in fractional atmospheric reflection r , absorption a , and effective sur-
 587 face albedo α depend on the region. r (primarily related to clouds) has the largest con-
 588 tribution in all regions with α (primarily related to snow cover) slightly offsetting the
 589 effect for North America and a (related to both water vapour and clouds) playing a larger
 590 role for PDO-related F_S^\downarrow anomalies in Europe and a smaller role for India and Indochi-
 591 nese peninsula. Magnitudes in F_T^\uparrow are in general less than those in F_S^\uparrow , which is explained
 592 by the increase of both r and a in those regions – increased atmospheric absorption slightly
 593 offsets the decrease in absorption at the surface.

594 The combined view through these different PDO lenses, ranging from a “realistic”
 595 PDO embedded in its natural context of other modes of variability in CMIP6 to a highly
 596 idealized, eternally phase locked PDO within our ICON-A simulations, inspires some hy-
 597 potheses and speculations. By assessing the similarities and differences in these patterns,
 598 we mark regions that show a different response in coupled and atmosphere-only simu-
 599 lations. The radiative flux anomalies in the South Pacific ocean evident in the idealized
 600 atmosphere-only simulations suggest that the North Pacific PDO impacts the South Pa-
 601 cific through changes in r (clouds). The resulting change in F_S^\downarrow (dimming and bright-
 602 ening) might be one of the mechanisms through which Northern extratropics commu-
 603 nicate with Southern extratropics and in the SST field: PDO and SPDO combine into
 604 IPO. We also note that a similar mechanism might be present for the North Atlantic –
 605 during a positive PDO phase, dimming over the East coast of North America (evident
 606 in the atmosphere-only simulations) can cool the surrounding waters, which in a cou-
 607 pled run are transported via ocean currents, resulting in dimming throughout the path

608 of the Gulf stream in the North Atlantic (as seen in the coupled simulations). Thus, un-
 609 forced decadal changes in the shortwave radiative fluxes, like dimming and brightening,
 610 appear to participate in sustaining (in the North Pacific) and maybe forcing (in the South
 611 Pacific and North Atlantic oceans) decadal scale SST trends, which highlights their im-
 612 portance for atmosphere-ocean modes in the coupled system.

613 Appendix A Appendix: Detailed experiment design

Here we give a detailed description of the modification we perform on the SST field used in the ICON-A simulations. We start by obtaining the monthly mean SSTs from the coupled ICON-ESM-LR piControl run that is 500 years of length. We take the temperature at the lower boundary of the atmosphere (surface temperature, t_s) that is already on the grid of the atmospheric model (R2B4, grid id 0013). We deseasonalize the data by subtracting the climatological mean for each month. We extract the surface temperature of non-land grid boxes using the ICON grid description and we arrange the SST field in a 2D matrix of time and space: $SST(t, x_{all})$, where $t \in [0; 6000)$ represents 500 years of monthly data and $x_{all} \in [0; 13132)$ represents all non-land grid boxes on the ICON grid. We further restrict the region of interest to the North Pacific bounding box: 20-70°N and 110-260°E. The resulting field $SST(t, x_{reg})$ with $x_{reg} \in [0, 1522)$, we decompose into a set of principal components $PC_i(t)$ and empirical orthogonal functions $EOF_i(x_{reg})$, weighted to the area of each grid box (singular value decomposition):

$$SST(t, x_{reg}) = \sum_{i=1}^{i_{max}} PC_i(t) \otimes EOF_i(x_{reg}), \quad (A1)$$

614 where $i_{max} = 1522$ corresponds to the number of grid boxes in x_{reg} . By definition, $PC_1(t)$
 615 and $EOF_1(x_{reg})$ correspond to the PDO time series and spatial pattern. The spatial pat-
 616 tern expressed as correlations is shown on Figure A1-a.

The main mathematical challenge is to have a smooth transition of the field outside the geographical box in which the EOF decomposition is performed (If the decomposition is performed on a larger box, the resulting EOF_1 bears the strong tropical fingerprint of ENSO.) In order to expand $EOF_1(x_{reg})$ into the larger domain, we use a method referred to as Empirical Orthogonal Function Teleconnections, or EOF Regression or Teleconnection Patterns (van den Dool et al., 2000). The method relies on expanding each $EOF_i(x_{reg})$ by computing the slope of linear regression between $SST(t, x_j)$ and $PC_i(t)$ for each grid box (x_j). The outer product of the obtained map of regression coefficients $s_i(x_{all})$ and $PC_i(t)$ gives us the reconstructed field for the i -th principal component:

$$\widetilde{SST}(t, x_{all}) = PC_i(t) \otimes s_i(x_{all}). \quad (A2)$$

In general, if we were to obtain a realistic field that represents a larger fraction of variability, we would have to obtain a linear regression coefficient map for each principal component and sum over all of them. Since our goal is to have a field containing variability only related to the first one, we simply:

$$\widetilde{SST}(t, x_{all}) = PC_1(t) \otimes s_1(x_{all}). \quad (A3)$$

617 This process uses the linear relationship between $SST(t, x)$ and $PC_1(t)$, contained in $s_1(x)$
 618 to reconstruct the field in the larger domain (x_{all}). By design, singular value decom-
 619 position represents the field as a linear combination of modes (eigenvectors), and their cor-
 620 responding PCs. Mathematically, the reconstruction yields identical results in the region
 621 of x_{reg} but extended to a larger domain. Since the decomposition is not done in the larger
 622 domain, we do not have the proper eigenvectors to reconstruct back the whole field but
 623 this is not our intention as we are only interested in the primary principal component
 624 and its extended eigenvector.

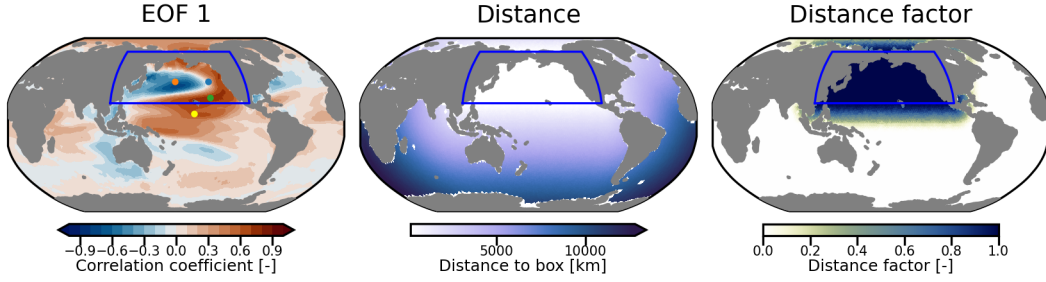


Figure A1. Left plot shows first EOF expressed as the correlation with the monthly SST time series for each grid box, blue box shows the region in which the EOF decomposition is done (same as on Figure 1. Superimposed points align with those presented in Figure A2. Middle plot shows the distance of each grid box from the boarder of the PDO box (blue box). Right plot shows the corresponding distance factor, obtained via the \sin^2 function. The distance factor equals 1 inside the box and 0 at distances exceeding 3000 km.

625 The idea of extending the spatial field from x_{reg} to x_{all} was for a smooth transi-
 626 tion of the projected field outside the boundaries of the North Pacific box. We do this
 627 by first computing the distance between the center of each grid box and the closest grid
 628 box within the North Pacific box: d . The resulting Distance map is shown on Figure A1-
 629 b. We decide on a maximum distance away from the region in which we modify the field
 630 of $d_{max} = 3000$ km. We construct a distance factor d_f that is:

$$d_f = \begin{cases} 1 & \text{if inside the N. Pacific box} \\ \sin\left(\frac{\pi}{2} \times \frac{d-d_{max}}{d_{max}}\right)^2 & \text{if } d < d_{max} \\ 0 & \text{if } d \geq d_{max} \end{cases} \quad (\text{A4})$$

631 The resulting d_f map is shown on Figure A1-c. When projecting an arbitrary $\widetilde{PC}_1(t)$
 632 in the form of anomaly time series to obtain a SST field, we simply multiply the time
 633 series by d_f . Climatological values per grid box are added in the end to obtain a real-
 634 istic field with seasonality.

635 We perform the following experiments, each 100 years of length:

- 636 1. “piSST”: SST taken directly from the coupled CMIP6 run. They correspond to
 637 the first 100 years (4001-4101) in the ICON-ESM-LR piControl simulation.
- 638 2. “lfPDO”: Project $\widetilde{PC}_1(t)$ that is obtained after low-pass filtering the original $PC_1(t)$
 639 with a filter in the form of a sharp logarithmic function in frequency space: $F =$
 640 $(a_1/a_0)^{f_i/(N-1)}$ for frequencies f_i higher than $f_{min} = 0.00833$ cycles/month, which
 641 corresponds to 10 years in monthly values. The coefficients are $a_1 = 10^{-7}$ and
 642 $a_0 = 1$. $N = 6000$ is the length of the input data in the form of deseasonalized
 643 monthly anomalies. The resulting $\widetilde{PC}_1(t)$ time series and its power spectra are
 644 shown on Figure 1. Its projection as SST anomalies is shown on Figure A2.
- 645 3. “Perpetual PDO” simulations, each corresponding to a different percentile (p) of
 646 the distribution of the original $PC_1(t)$ monthly values and we project a constant
 647 in time $\widetilde{PC}_1(t)$:
 648 (a) $\widetilde{PC}_1(t) = const = 2.58$ (p99)
 649 (b) $\widetilde{PC}_1(t) = const = 1.64$ (p95)
 650 (c) $\widetilde{PC}_1(t) = const = 0.44$ (p68)

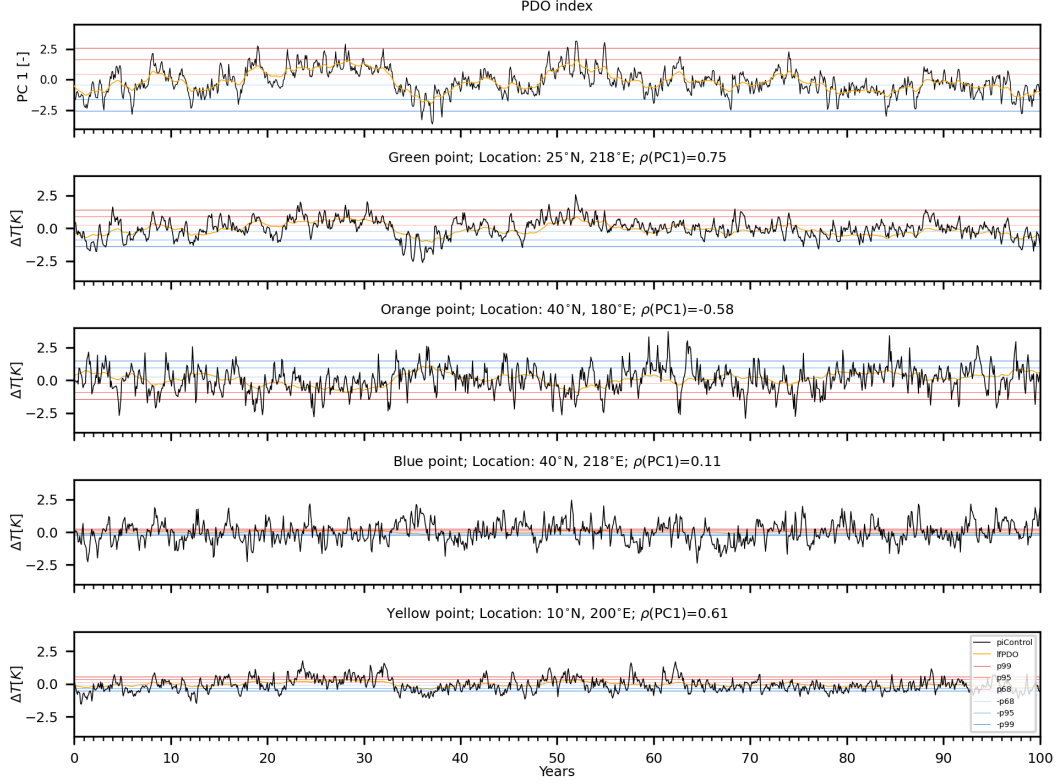


Figure A2. Time series of the first principal component and deseasonalized monthly SST anomalies at different locations, depicted on Figure A1 for 100 years. The green point as chosen with a strong positive correlation with PC1 ($\rho(\text{PC1})$), the orange point – with a strong negative, the blue point – weak correlation. The yellow point is strongly correlated to PC1 but lies outside the analysis box and is affected by the distance factor. Black curve shows the original SST time series from the piControl run (also the control simulation), orange curve shows time series from SST field after projecting the low-pass filtered PC1. Gray lines depict the climatological simulation (all values are zero), blue lines depict locked negative phase PDO simulations and red lines – locked positive phase PDO simulations. Seasonality is not shown on the plots but included in the SST boundary conditions.

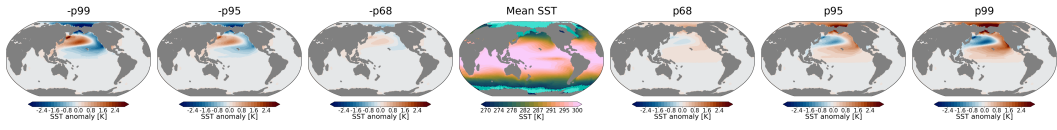


Figure A3. SST anomaly associated with different percentiles (p) of the monthly PDO index distribution that we uses for the corresponding experiments. Middle plot shows the mean SST field on top of which we add the anomalies and the three shades of turquoise represent the maximum, mean and minimum extent of sea ice within one year.

- 651 (d) $\widetilde{PC}_1(t) = \text{const} = 0$ (p50, control run)
 652 (e) $\widetilde{PC}_1(t) = \text{const} = -0.44$ (-p68)
 653 (f) $\widetilde{PC}_1(t) = \text{const} = -1.64$ (-p95)
 654 (g) $\widetilde{PC}_1(t) = \text{const} = -2.58$ (-p99)

655 For a better illustration of how the SST field is being modified for each experiment,
656 we include the anomaly time series (before adding the seasonality) for different grid boxes
657 on Figure A2. The locations of the points are shown on Figure A1-a and we choose them
658 as: the green point represents a location with a strong positive correlation with the $PC_1(t)$
659 time series; the orange point - strong negative correlation; the blue point is within the
660 North Pacific box but is not correlated with the $PC_1(t)$ time series; and the yellow point
661 is strongly correlated with the $PC_1(t)$ time series but lies outside the North Pacific box
662 and is therefore again weakly affected by our modification (projected anomalies are smaller
663 in magnitude as compared to the green and orange points). The spatial representation
664 for each of the $\widetilde{PC}_1(t) = const$ projections is given on Figure A3, where we also show
665 the mean SST field and the climatology of sea ice that is kept constant across simula-
666 tions, i.e. does not exhibit any inter-annual variability.

667

Appendix B Appendix: Patterns for ICON-ESM-LR

668

669

670

671

The all-sky and clear-sky shortwave flux and cloud radiative effect trend patterns during 20-year periods with a strong phase transition of the PDO index for ICON-ESM-LR are shown to complement the patterns of the multi-model median of CMIP6 in Figures 2-3.

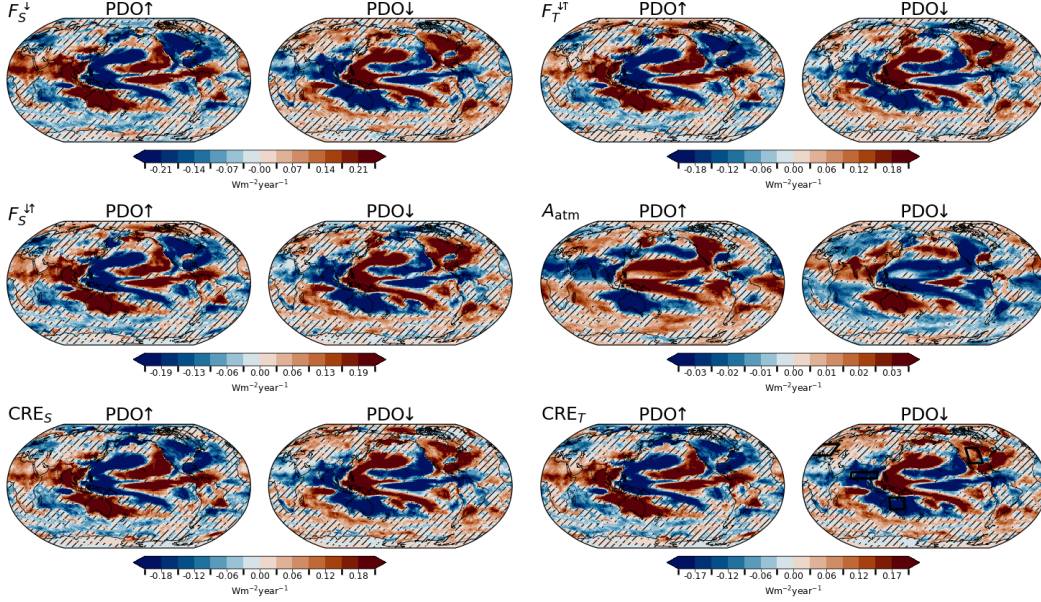


Figure B1. Same as Figure 2 but only for the piControl simulation of ICON-ESM-LR.

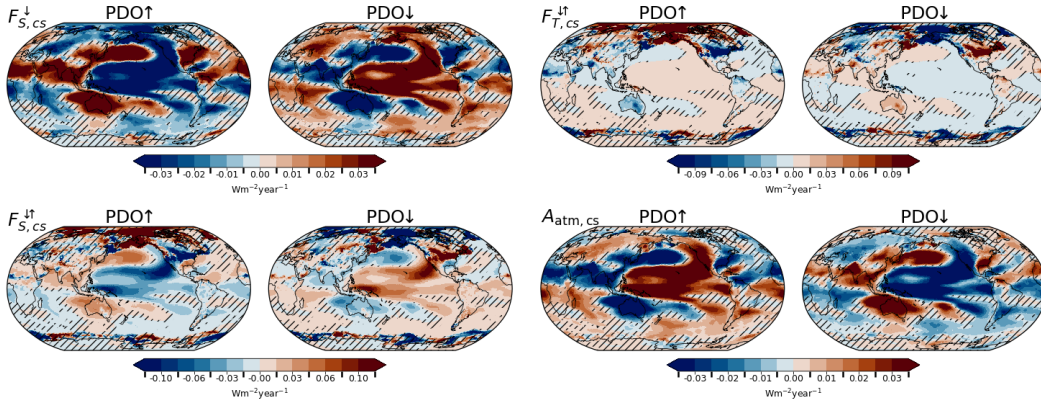


Figure B2. Same as Figure 3 but only for the piControl simulation of ICON-ESM-LR.

672

Open Research Section

673

674

675

676

677

Data from the Coupled Model Inter-comparison Project—Phase 6 were used in the manuscript (Eyring et al., 2016). Climate indices were computed using the Climate variability diagnostics package (CVDP) (Phillips et al., 2014). Observational sea surface temperatures are taken from the NOAA Extended Reconstructed SST V5 (ERSST) (Huang et al., 2017).

Acknowledgments

This work was funded by Swiss National Science Foundation Grant 200020_188601. The numerical simulations were realized through a grant from the Swiss National Supercomputing Centre (CSCS) under project ID s1144. We acknowledge the World Climate Research Programme, which, through its Working Group on Coupled Modelling, coordinated and promoted CMIP6. We thank the climate modeling groups for producing and making available their model output, the Earth System Grid Federation (ESGF) for archiving the data and providing access, and the multiple funding agencies who support CMIP6 and ESGF. The data analysis and visualization have been performed using exclusively free and open source software (including Linux, Python, and CDO): we would like to thank the community for building powerful tools from which everyone can benefit.

References

- Allan, R. P., Liu, C., Loeb, N. G., Palmer, M. D., Roberts, M., Smith, D., & Vidale, P.-L. (2014, aug). Changes in global net radiative imbalance 1985–2012. *Geophysical Research Letters*, *41*(15), 5588–5597. Retrieved from <https://doi.org/10.1002/2014gl060962> doi: 10.1002/2014gl060962
- Augustine, J. A., & Capotondi, A. (2022, aug). Forcing for multidecadal surface solar radiation trends over northern hemisphere continents. *Journal of Geophysical Research: Atmospheres*, *127*(16). Retrieved from <https://doi.org/10.1029/2021jd036342> doi: 10.1029/2021jd036342
- Chen, X., & Wallace, J. M. (2015, dec). ENSO-like variability: 1900–2013*. *Journal of Climate*, *28*(24), 9623 – 9641. Retrieved from <https://doi.org/10.1175/jcli-d-15-0322.1> doi: 10.1175/jcli-d-15-0322.1
- Chtirkova, B., Folini, D., Correa, L. F., & Wild, M. (2022, jun). Internal variability of all-sky and clear-sky surface solar radiation on decadal timescales. *Journal of Geophysical Research: Atmospheres*, *127*(12). Retrieved from <https://doi.org/10.1029/2021jd036332> doi: 10.1029/2021jd036332
- Chtirkova, B., Folini, D., Correa, L. F., & Wild, M. (2023, jun). Internal variability of the climate system mirrored in decadal-scale trends of surface solar radiation. *Journal of Geophysical Research: Atmospheres*, *128*(12). Retrieved from <https://doi.org/10.1029/2023jd038573> doi: 10.1029/2023jd038573
- Crueger, T., Giorgetta, M. A., Brokopf, R., Esch, M., Fiedler, S., Hohenegger, C., . . . Stevens, B. (2018, jul). ICON-a, the atmosphere component of the ICON earth system model: II. model evaluation. *Journal of Advances in Modeling Earth Systems*, *10*(7), 1638–1662. Retrieved from <https://doi.org/10.1029/2017ms001233> doi: 10.1029/2017ms001233
- Donohoe, A., Armour, K. C., Pendergrass, A. G., & Battisti, D. S. (2014, nov). Short-wave and longwave radiative contributions to global warming under increasing CO₂. *Proceedings of the National Academy of Sciences*, *111*(47), 16700–16705. Retrieved from <https://doi.org/10.1073/pnas.1412190111> doi: 10.1073/pnas.1412190111
- Eyring, V., Bony, S., Meehl, G. A., Senior, C. A., Stevens, B., Stouffer, R. J., & Taylor, K. E. (2016, may). Overview of the coupled model intercomparison project phase 6 (CMIP6) experimental design and organization. *Geoscientific Model Development*, *9*(5), 1937–1958. Retrieved from <https://doi.org/10.5194/gmd-9-1937-2016> doi: 10.5194/gmd-9-1937-2016
- Folini, D., Dallafior, T. N., Hakuba, M. Z., & Wild, M. (2017, jan). Trends of surface solar radiation in forced CMIP5 simulations. *Journal of Geophysical Research: Atmospheres*, *122*(1), 469–484. Retrieved from <https://doi.org/10.1002/2016jd025869> doi: 10.1002/2016jd025869

- 726 Folland, C. K. (2002). Relative influences of the interdecadal pacific oscillation and
 727 ENSO on the south pacific convergence zone. *Geophysical Research Letters*, *29*(13). Re-
 728 trieved from <https://doi.org/10.1029%2F2001gl1014201> doi: 10.1029/2001gl1014201
 729
- 730 Giorgetta, M. A., Brokopf, R., Crueger, T., Esch, M., Fiedler, S., Helmert, J., ... Stevens,
 731 B. (2018, jul). ICON-a, the atmosphere component of the ICON earth system model:
 732 I. model description. *Journal of Advances in Modeling Earth Systems*, *10*(7), 1613–1637.
 733 Retrieved from <https://doi.org/10.1029%2F2017ms001242> doi: 10.1029/2017ms001242
 734
- 735 Harris, C. R., Millman, K. J., van der Walt, S. J., Gommers, R., Virtanen, P., Cournapeau,
 736 D., ... Oliphant, T. E. (2020, September). Array programming with NumPy.
 737 *Nature*, *585*(7825), 357–362. Retrieved from <https://doi.org/10.1038/s41586-020-2649-2>
 738 doi: 10.1038/s41586-020-2649-2
- 739 Henley, B. J., Gergis, J., Karoly, D. J., Power, S., Kennedy, J., & Folland, C. K. (2015,
 740 mar). A tripole index for the interdecadal pacific oscillation. *Climate Dynamics*, *45*(11-
 741 12), 3077–3090. Retrieved from <https://doi.org/10.1007%2Fs00382-015-2525-1> doi:
 742 10.1007/s00382-015-2525-1
- 743 Huang, B., Thorne, P. W., Banzon, V. F., Boyer, T., Chepurin, G., Lawrimore, J. H.,
 744 ... Zhang, H.-M. (2017). *[dataset] noaa extended reconstructed sea surface tempera-*
 745 *ture (ersst), version 5*. NOAA National Centers for Environmental Information. Re-
 746 trieved from <https://data.nodc.noaa.gov/cgi-bin/iso?id=gov.noaa.ncdc:C00927>
 747 doi: 10.7289/V5T72FNM
- 748 IPCC. (2021). *Climate change 2021: The physical science basis. contribution of work-*
 749 *ing group i to the sixth assessment report of the intergovernmental panel on climate change*
 750 [Book]. Cambridge, United Kingdom and New York, NY, USA: Cambridge University
 751 Press. Retrieved from <https://www.ipcc.ch/report/ar6/wg1/>
- 752 Jungclaus, J. H., Lorenz, S. J., Schmidt, H., Brovkin, V., Brüggemann, N., Chegini, F.,
 753 ... Claussen, M. (2022, apr). The ICON earth system model version 1.0. *Journal of*
 754 *Advances in Modeling Earth Systems*, *14*(4). Retrieved from [https://doi.org/10.1029%](https://doi.org/10.1029%2F2021ms002813)
 755 [2F2021ms002813](https://doi.org/10.1029/2021ms002813) doi: 10.1029/2021ms002813
- 756 Liu, Z., Tang, Y., Jian, Z., Poulsen, C. J., Welker, J. M., & Bowen, G. J. (2017, mar).
 757 Pacific north american circulation pattern links external forcing and north american hy-
 758 droclimatic change over the past millennium. *Proceedings of the National Academy of*
 759 *Sciences*, *114*(13), 3340–3345. Retrieved from <https://doi.org/10.1073%2Fpnas.1618201114>
 760 doi: 10.1073/pnas.1618201114
- 761 Loeb, N. G., Johnson, G. C., Thorsen, T. J., Lyman, J. M., Rose, F. G., & Kato, S. (2021,
 762 July). Satellite and ocean data reveal marked increase in earth’s heating rate. *Geo-*
 763 *physical Research Letters*, *48*(13). Retrieved from <https://doi.org/10.1029/2021gl1093047>
 764 doi: 10.1029/2021gl1093047
- 765 Loeb, N. G., Thorsen, T., Norris, J., Wang, H., & Su, W. (2018, July). Changes in
 766 earth’s energy budget during and after the “pause” in global warming: An observational
 767 perspective. *Climate*, *6*(3), 62. Retrieved from <https://doi.org/10.3390/cli6030062>
 768 doi: 10.3390/cli6030062
- 769 Loeb, N. G., Wang, H., Rose, F. G., Kato, S., Smith, W. L., & Sun-Mack, S. (2019, jul).
 770 Decomposing shortwave top-of-atmosphere and surface radiative flux variations in terms
 771 of surface and atmospheric contributions. *Journal of Climate*, *32*(16), 5003–5019. Re-
 772 trieved from <https://doi.org/10.1175%2Fjcli-d-18-0826.1> doi: 10.1175/jcli-d-18-
 773 -0826.1

- 774 Mann, H. B., & Whitney, D. R. (1947, March). On a test of whether one of two ran-
 775 dom variables is stochastically larger than the other. *The Annals of Mathematical Statis-*
 776 *tics*, 18(1), 50–60. Retrieved from <https://doi.org/10.1214/aoms/1177730491> doi:
 777 10.1214/aoms/1177730491
- 778 Mantua, N. J., & Hare, S. R. (2002).
 779 *Journal of Oceanography*, 58(1), 35–44. Retrieved from [https://doi.org/10](https://doi.org/10.1023%2Fa%3A1015820616384)
 780 [.1023%2Fa%3A1015820616384](https://doi.org/10.1023/a:1015820616384) doi: 10.1023/a:1015820616384
- 781 Meyssignac, B., Chenal, J., Loeb, N., Guillaume-Castel, R., & Ribes, A. (2023, jul). Time-
 782 variations of the climate feedback parameter are associated with the pacific decadal os-
 783 cillation. *Communications Earth & Environment*, 4(1). Retrieved from [https://](https://doi.org/10.1038%2Fs43247-023-00887-2)
 784 doi.org/10.1038/s43247-023-00887-2 doi: 10.1038/s43247-023-00887-2
- 785 Newman, M., Alexander, M. A., Ault, T. R., Cobb, K. M., Deser, C., Lorenzo, E. D.,
 786 ... Smith, C. A. (2016, jun). The pacific decadal oscillation, revisited. *Journal of*
 787 *Climate*, 29(12), 4399–4427. Retrieved from [https://doi.org/10.1175%2Fjcli-d-15](https://doi.org/10.1175%2Fjcli-d-15-0508.1)
 788 [-0508.1](https://doi.org/10.1175/jcli-d-15-0508.1) doi: 10.1175/jcli-d-15-0508.1
- 789 Phillips, A. S., Deser, C., & Fasullo, J. (2014). [software] a new tool for evaluating modes
 790 of variability in climate models. *EOS*, 95, 453–455. Retrieved from [https://www.cesm](https://www.cesm.ucar.edu/working_groups/CVC/cvdp/)
 791 [.ucar.edu/working_groups/CVC/cvdp/](https://www.cesm.ucar.edu/working_groups/CVC/cvdp/) doi: 10.1002/2014EO490002
- 792 Pinto, J. G., Reyers, M., & Ulbrich, U. (2010, mar). The variable link between PNA
 793 and NAO in observations and in multi-century CGCM simulations. *Climate Dynam-*
 794 *ics*, 36(1-2), 337–354. Retrieved from [https://doi.org/10.1007%2Fs00382-010-0770](https://doi.org/10.1007%2Fs00382-010-0770-x)
 795 [-x](https://doi.org/10.1007/s00382-010-0770-x) doi: 10.1007/s00382-010-0770-x
- 796 Power, S., Casey, T., Folland, C., Colman, A., & Mehta, V. (1999, may). Inter-decadal
 797 modulation of the impact of ENSO on australia. *Climate Dynamics*, 15(5), 319–324.
 798 Retrieved from <https://doi.org/10.1007%2Fs003820050284> doi: 10.1007/s003820050284
 799
- 800 Qiu, B., Schneider, N., & Chen, S. (2007, jul). Coupled decadal variability in the north
 801 pacific: An observationally constrained idealized model*. *Journal of Climate*, 20(14), 3602 – –3620. Retrieved from
 802 doi: 10.1175/jcli4190.1
- 803 Rohli, R. V., Snedden, G. A., Martin, E. R., & DeLong, K. L. (2022, aug). Impacts
 804 of ocean-atmosphere teleconnection patterns on the south-central united states. *Fron-*
 805 *tiers in Earth Science*, 10. Retrieved from [https://doi.org/10.3389%2Ffeart.2022](https://doi.org/10.3389%2Ffeart.2022.934654)
 806 [.934654](https://doi.org/10.3389/feart.2022.934654) doi: 10.3389/feart.2022.934654
- 807 Schneider, D. P., Deser, C., Fasullo, J., & Trenberth, K. E. (2013, mar). Climate data
 808 guide spurs discovery and understanding. *Eos, Transactions American Geophysical Union*,
 809 94(13), 121–122. Retrieved from <https://doi.org/10.1002%2F2013eo130001> doi:
 810 [10.1002/2013eo130001](https://doi.org/10.1002/2013eo130001)
- 811 Shakun, J. D., & Shaman, J. (2009, oct). Tropical origins of north and south pacific
 812 decadal variability. *Geophysical Research Letters*, 36(19). Retrieved from [https://](https://doi.org/10.1029%2F2009gl040313)
 813 doi.org/10.1029/2009gl040313 doi: 10.1029/2009gl040313
- 814 Simon, A., Gastineau, G., Frankignoul, C., Lapin, V., & Ortega, P. (2022, aug). Pa-
 815 cific decadal oscillation modulates the arctic sea-ice loss influence on the midlatitude at-
 816 mospheric circulation in winter. *Weather and Climate Dynamics*, 3(3), 845–861. Re-
 817 trieved from <https://doi.org/10.5194%2Fwcd-3-845-2022> doi: 10.5194/wcd-3-845
 818 -2022

- 819 Stanhill, G., & Moreshet, S. (1992, may). Global radiation climate changes: The world
820 network. *Climatic Change*, *21*(1), 57–75. Retrieved from [https://doi.org/10.1007/](https://doi.org/10.1007/2Fbf00143253)
821 [2Fbf00143253](https://doi.org/10.1007/bf00143253) doi: 10.1007/bf00143253
- 822 Stephens, G. L., O'Brien, D., Webster, P. J., Pilewski, P., Kato, S., & Lin Li, J. (2015,
823 mar). The albedo of earth. *Reviews of Geophysics*, *53*(1), 141–163. Retrieved from
824 <https://doi.org/10.1002/2F2014rg000449> doi: 10.1002/2014rg000449
- 825 Student. (1908, 03). The probable error of a mean. *Biometrika*, *6*(1), 1–25. Retrieved
826 from <https://doi.org/10.1093/biomet/6.1.1> doi: 10.1093/biomet/6.1.1
- 827 Taguchi, B., Xie, S.-P., Schneider, N., Nonaka, M., Sasaki, H., & Sasai, Y. (2007, jun).
828 Decadal variability of the kuroshio extension: Observations and an eddy-resolving model
829 hindcast*. *Journal of Climate*, *20*(11), 2357 – 2377. Retrieved from doi: 10.1175/
830 jcli4142.1
- 831 Trenberth, K. E., & Fasullo, J. T. (2009, apr). Global warming due to increasing ab-
832 sorbed solar radiation. *Geophysical Research Letters*, *36*(7), n/a–n/a. Retrieved from
833 <https://doi.org/10.1029/2F2009gl037527> doi: 10.1029/2009gl037527
- 834 van den Dool, H. M., Saha, S., & Johansson, Å. (2000, April). Empirical orthogonal
835 teleconnections. *Journal of Climate*, *13*(8), 1421–1435. Retrieved from [https://doi](https://doi.org/10.1175/1520-0442(2000)013<1421:eot>2.0.co;2)
836 [.org/10.1175/1520-0442\(2000\)](https://doi.org/10.1175/1520-0442(2000)013<1421:eot>2.0.co;2)
837 [013\(1421:eot\)2.0.co;2](https://doi.org/10.1175/1520-0442(2000)013<1421:eot>2.0.co;2) doi: 10.1175/1520-0442(2000)
- 838 Welch, P. (1967, jun). The use of fast fourier transform for the estimation of power
839 spectra: A method based on time averaging over short, modified periodograms. *IEEE*
840 *Transactions on Audio and Electroacoustics*, *15*(2), 70–73. Retrieved from [https://](https://doi.org/10.1109/2Ftau.1967.1161901)
841 doi.org/10.1109/2Ftau.1967.1161901 doi: 10.1109/tau.1967.1161901
- 842 Wild, M. (2009, June). Global dimming and brightening: A review. *Journal of Geo-*
843 *physical Research*, *114*. Retrieved from <https://doi.org/10.1029/2008jd011470> doi:
844 [10.1029/2008jd011470](https://doi.org/10.1029/2008jd011470)
- 845 Wild, M., Folini, D., Hakuba, M. Z., Schär, C., Seneviratne, S. I., Kato, S., ... König-
846 Langlo, G. (2014, dec). The energy balance over land and oceans: an assessment based
847 on direct observations and CMIP5 climate models. *Clim Dyn*, *44*(11-12), 3393–3429.
848 Retrieved from <https://doi.org/10.1007/2Fs00382-014-2430-z> doi: 10.1007/s00382
849 [-014-2430-z](https://doi.org/10.1007/s00382-014-2430-z)
- 850 Wild, M., Folini, D., Schär, C., Loeb, N., Dutton, E. G., & König-Langlo, G. (2012, nov).
851 The global energy balance from a surface perspective. *Climate Dynamics*, *40*(11-12),
852 3107–3134. Retrieved from <https://doi.org/10.1007/2Fs00382-012-1569-8> doi:
853 [10.1007/s00382-012-1569-8](https://doi.org/10.1007/s00382-012-1569-8)
- 854 Wills, R. C. J., Armour, K. C., Battisti, D. S., Proistosescu, C., & Parsons, L. A. (2021,
855 November). Slow modes of global temperature variability and their impact on climate
856 sensitivity estimates. *Journal of Climate*, *34*(21), 8717–8738. Retrieved from [https://](https://doi.org/10.1175/jcli-d-20-1013.1)
857 doi.org/10.1175/jcli-d-20-1013.1 doi: 10.1175/jcli-d-20-1013.1
- 858 Wills, R. C. J., Battisti, D. S., Proistosescu, C., Thompson, L., Hartmann, D. L., & Ar-
859 mour, K. C. (2019, feb). Ocean circulation signatures of north pacific decadal vari-
860 ability. *Geophysical Research Letters*, *46*(3), 1690–1701. Retrieved from [https://doi](https://doi.org/10.1029/2F2018gl080716)
861 [.org/10.1029/2F2018gl080716](https://doi.org/10.1029/2F2018gl080716) doi: 10.1029/2018gl080716
- 862 Zhang, Y., Xie, S.-P., Kosaka, Y., & Yang, J.-C. (2018, oct). Pacific decadal oscilla-
863 tion: Tropical pacific forcing versus internal variability. *Journal of Climate*, *31*(20), 8265–

864 8279. Retrieved from <https://doi.org/10.1175%2Fjcli-d-18-0164.1> doi: 10.1175/
865 jcli-d-18-0164.1

866 Zheng, Z. (2021, February). *zzheng93/pyeof: First release*. Zenodo. Retrieved from
867 <https://doi.org/10.5281/zenodo.4556051> doi: 10.5281/zenodo.4556051